Rare-Gas Solvent Clusters: Spectra, Structures, and Order–Disorder Transitions

SAMUEL LEUTWYLER* and JÜRG BÖSIGER

Institut für Anorganische, Analytische und Physikalische Chemie, Freiestr. 3, CH-3000 Bern 9, Switzerland

Received September 28, 1988 (Revised Manuscript Received December 1, 1989)

Contents

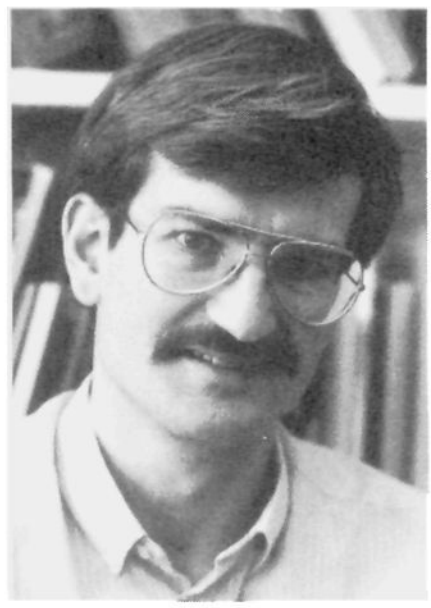

Samuel Leutwyler studied chemistry at the University of Bern. His thesis work with Prof. E. Schumacher concerned molecular-beam and matrix spectroscopy of alkali-metal clusters. After receiving his Ph.D. degree (1979), he did postdoctoral work with Profs. Uzi Even and Joshua Jortner at Tel-Aviv University. From 1981 to 1984 he was a research associate at the Physikalisch-Chemisches Institut of the University of Basel, where he obtained his Habilitation in 1984. He moved to the University of Bern the same year, where he was appointed Privatdozent. In 1986, he received the Haber-Preis of the Deutsche Bunsen-Gesellschaft für Physikalische Chemie. His current research interests concern the physics and chemistry of isolated clusters as well as laser synthesis of ultrafine particles.

Jürg Bösiger was born in 1961 in Solothurn, Switzerland. He studied chemistry at the University of Bern and received his Diploma in biochemistry in 1985, working with Prof. Baggiolini. His graduate work involved both experimental and theoretical studies on rare-gas clusters. He obtained his Ph.D. in 1988.

1. Introduction

Spectroscopy provides a variety of experimental routes for the exploration of the structures of molecules and of intra- and intermolecular vibrations and binding energies. While the spectroscopy of isolated molecules and crystalline solids is highly advanced, there is a terra incognita between the isolated molecule and the bulk limits that remains to be explored by investigating finite systems such as atomic or molecular clusters. A detailed understanding of the physics and chemistry of clusters would also allow a more precise description of liquids, amorphous solids, and disordered materials, for which our present knowledge is still fairly rudimentary.

One possible approach to the spectroscopy of clusters is to study doped or (in chemical terms) solute–solvent clusters, i.e., clusters that contain a *probe* atom or molecule.[1-39] The physical properties of the cluster are reflected by the spectroscopic properties of the probe via the cluster–probe interaction.[11,24,26,27,29-37] On the other hand, doped clusters provide paradigmatic sys-

0009-2665/90/0790-0489$09.50/0

tems for the study of solvent influence on localized electronic[11,23,30] or vibrational[38-40] excitations of the solute.

Many questions arise when an attempt is made to describe solvent clusters or the solvation process on an atomic scale: What are the solvent cluster structures?[24,29,32-37] To what extent is the structure of the solvent cluster representative of the undoped cluster? Does the solute imprint its shape on its microsolvent surroundings, i.e., control the solvent cluster structure? Do solvation isomers exist, and are they energetically competitive with the minimum-energy structure? How strong are the interactions that are responsible for solvation? To what extent do the cluster structures depend on temperature? Are the clusters solidlike (rigid) or liquidlike (fluxional), and can solid–liquid transitions be observed?[32-34,36,39-47] Is it possible to identify the first and successive solvent layers? Is it possible to see the appearance of bulklike behavior already in finite clusters?

We will attempt to answer these questions by discussing recent experimental and theoretical results that concern the structural and dynamical properties of $M{\cdot}R_n$ clusters, where R is a rare-gas atom and M is the large planar aromatic molecule carbazole:

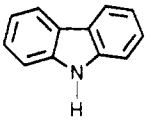

In these systems, solvation effects can be investigated at the atomic level: starting from an isolated aromatic molecule M that is cooled in a supersonic beam, solvent atoms or molecules R are added one by one to form solvent clusters $M{\cdot}R_n$ with n up to 100.[32-36]

Rare-gas solvents exhibit a number of properties that simplify the theoretical treatment: First, the solute–solvent interaction is dominated by pairwise additive two-body forces; typically, these account for 90–95% of the total solvent–solvent interaction energy.[48-50] Second, the solvent–solvent potentials have been studied extensively. The rare-gas two-body potentials are isotropic and are experimentally known to high precision.[51,52] The remaining many-body interaction terms are well approximated by the Axilrod–Teller triple-dipole polarization terms, with higher terms canceling out to a high degree.[48-50] Third, the first and higher electronic excitations of the solvent (typically at 10–12 eV[49]) are well removed from the first electronic transition of the solute, which typically lies at ≈3 eV. This makes it possible to treat the solvent-induced electronic spectral shifts by perturbation theory[11,17,23,30] and allows one to neglect charge-transfer-type excitations to the solvent following electronic excitation of the solute.

Several excellent reviews covering dynamic, thermodynamic, structural, and computational aspects of weakly bound dimers and clusters have appeared in a thematic issue of this journal on van der Waals interactions (*Chem. Rev.* **1988**, *88*(6)), and we urge the reader to refer to this issue for a broader view of the subject of weak intermolecular interactions.

The experimental methods typically encompass laser spectroscopic techniques such as fluorescence excitation and emission spectroscopy[1-11] and resonant two-photon ionization spectroscopy (R2PI).[12-14,18] These methods allow one to measure electronic absorption and emission spectra of *size-selected clusters* and hence to follow the size dependence of the spectral properties. The major effects of the solvent clusters on the solute electronic absorption spectra is to shift the peak locations, to broaden the width of the bands, and to change the band shapes. Some key experimental findings are that the changes may be very specific and highly dependent on cluster size, and the trends in the band shifts, bandwidths, and band shapes can be very nonmonotonic.[32-34,36] It follows that the underlying solute–solvent interactions, even for such simple solvents as rare gases, must be size specific. A qualitative interpretation of the spectra also reveals that certain solvent clusters must exist as fairly localized, rigid-molecule structures, while other clusters of different size must be fluxional or liquidlike. Furthermore, some solvent clusters seem to be able to exist in both forms at the same temperature, and the transition between the solidlike and liquidlike states takes place within a finite temperature range.[33,34,36]

On the theoretical side, both molecular dynamics[53] and Monte Carlo[54,55] methods have been employed to simulate constant-energy or constant-temperature properties of the solvent cluster ensembles.[32-36,39,40] The simulations yield detailed insight into the structural and dynamic properties of the solvent clusters.

Typically, in small clusters ($n \leq 3$) the simulations predict one dominant cluster structure. However, the number of energetically accessible cluster isomers rises very rapidly with n and can soon become astronomical. If the energy barriers between isomers are low, then isomerization may become significant, even at very low internal temperatures. Qualitatively different types of cluster structures are also predicted by the simulations: single-sided monolayer structures, in which the raftlike solvent cluster adsorbs onto one microsurface of the substrate molecule, or double-sided structures, in which the solute is sandwiched between two layers of solvent; bilayer structures are also important for certain size ranges.

Considering the dynamical results of the simulations, it is found that the short-range ordering of the solvent layer which is induced by the solute–solvent and solvent–solvent interactions at low temperature decreases with increasing temperature. A remarkable result of the simulations is that a series of order–disorder transitions occurs, in which the low-temperature solidlike clusters are converted to the liquidlike state in several distinct stages. The different order–disorder transitions reflect the successive loss of different types of order.

We note that the study of melting transitions in clusters and small particles is also important in its own right, since it leads to a deeper microscopic understanding of the solid–liquid phase transition. A central issue in this area is the size dependence of the melting transition temperature. The melting points of small particles have long been predicted to decrease with decreasing particle size.[56,57] Several molecular dynamics (MD) and Monte Carlo (MC) simulation studies on Ar_n clusters (n = 3–100) have found size-dependent and sharp melting transitions.[41-43] Another issue of importance is the width and shape of the transition in finite systems. Berry et al. have predicted by quantum statistical model calculations that clusters should show

unequal freezing and melting temperatures T_f and T_m and a coexistence range (T_f, T_m) over which both solidlike and liquidlike forms should coexist.[44,45] This prediction is supported by MD and MC studies on Ar_n clusters.[46,47]

2. Experimental and Theoretical Methods

2.1. Laser Spectroscopic Techniques

Electronic spectra of M·R_n rare-gas solvent clusters have been measured by various laser spectroscopic techniques. A number of experimental studies have shown that laser-induced fluorescence excitation (LIF) spectroscopy can be employed as a sensitive tool for probing symmetries, structures, and intermolecular vibrations of rare-gas solvent clusters. Extensively studied systems are tetracene·R_n (n = 1–7),[5,6,9–11,19–21] pentacene·Ar_n (n = 1–3),[7,10,11] anthracene·Ar_n (n = 1–10),[10,14,15] fluorene·R_n (n = 1–3),[8,11–13] perylene·R_n (n = 1–5),[24,29] and 9,10-dichloroanthracene·R_n (n = 1–20).[22,70] In the large cluster size range, M·Ar_n clusters with M = anthracene, tetracene, and pentacene and unspecified n (≥6) have been studied; these large clusters exhibit broad, unstructured LIF excitation features.[9,10]

There are two drawbacks associated with LIF spectroscopy: first, the technique is not inherently species sensitive, i.e., does not give direct information on composition and size of the clusters, and assignments have to rely on subsidiary experimental information (pressure dependence, order of appearance); second, it is not possible to discriminate between cluster species with overlapping absorption spectra.

More recently, resonant two-photon ionization (R2PI) spectroscopy combined with mass spectrometric detection has been applied.[12,13,16,18] A diagram showing the R2PI scheme as applied to vibronic excitations of a bare substrate molecule M and the van der Waals complex M·R is shown in Figure 1. The systems studied include fluorene·R_n,[11–13] fluorobenzene·R_n,[25] phenylacetylene·R_n,[27] *p*-xylene·R_n,[28] benzene·R_n,[71] and carbazole·R_n.[31–34,36] The R2PI method provides a method for mass- and thus genuinely size-specific measurement of cluster spectra. Complications due to cluster fragmentation are not always negligible[71] but can often be avoided or minimized by using two photons of different frequency[34,36,71a] (see Figure 1).

The present review concentrates on the carbazole·Ar_n data, since in this system cluster fragmentation is negligible under carefully controlled conditions;[31,32,36] thus, cluster sizes are unequivocally determined, and size-specific electronic spectra are obtained. Also, it proved possible to obtain a contiguous series of electronic spectra of clusters with n = 1–36. The near-UV $S_1 \leftarrow S_0$ ($^1A_1 \leftarrow {}^1A_1$) transition of the carbazole solute molecule was used to interrogate the effects of solvation. Experimental details have been given in previous work.[31–36]

2.2. Intermolecular Potentials and Computer Simulation Methods

In order to extract maximum information from the spectral band shifts and band shapes, it is necessary to gain a detailed understanding of the structural and dynamical properties of the solvent clusters, both at 0 K and at finite temperatures. The theoretical basis for the calculation and simulation of these systems is threefold:

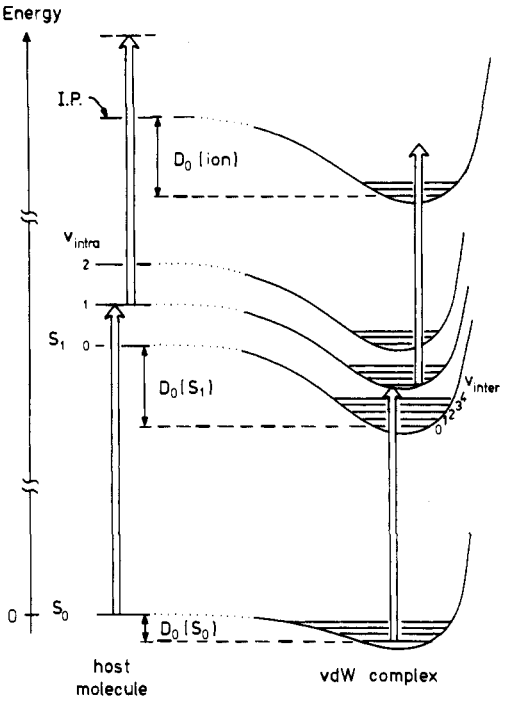

Figure 1. Schematic diagram of the resonant two-photon ionization (R2PI) process for an aromatic host molecule M (left side) and the corresponding rare-gas van der Waals complex M·R (right side). Ground- and excited-state electronic levels (S_0 and S_1) and the ionization potential (IP) are indicated. Intramolecular vibrational levels of the host molecule, marked by ν_{intra}, are correlated with corresponding levels in the van der Waals complex; the latter has three additional *intermolecular vibrational* degrees of freedom, marked by ν_{inter}. For one of these degrees of freedom, the perpendicular or out-of-plane M–R vibration, schematic intermolecular potentials are drawn. Note that the dissociation energy D_0 of the van der Waals complex depends on the electronic state and that $D_0(S_1) > D_0(S_0)$, which leads to the red shift of the electronic origins in the M·R_n clusters.

(*i*) *Intermolecular Potentials.* The total interaction between the aromatic molecule and the rare-gas atoms is represented by pairwise summation of atom–atom model potentials,[11,35,37] i.e., the effective two-body interactions V_{RC}, V_{RH}, and V_{RR} between R and each C and H atom in the molecule (indices c and h) and each R atom in the solvent cluster (index i).

$$V_{tot}(r_{ic},r_{ih},r_{ij}) = \sum_i\sum_c V_{RC}(r_{ic}) + \sum_i\sum_h V_{RH}(r_{ih}) + \sum_{i<j}\sum V_{RR}(r_{ij})$$

V_{RC}, V_{RH}, and V_{RR} are modeled by Lennard-Jones potential functions, e.g.

$$V_{RC}(r_{ic}) = 4\epsilon_{RC}[(\sigma_{RC}/r_{ic})^{12} - (\sigma_{RC}/r_{ic})^6]$$

This ansatz for intermolecular potentials has been widely applied for the calculation of the physisorption interactions of inert gases with the graphite basal plane and was introduced and extended to the study of M·R_n complexes by Ondrechen et al.[37] This effective two-body potential can be rapidly computed, providing a basis for the following two methods as well as for evaluating complete potential energy surfaces, equilibrium structures, vibrational frequencies, etc. Reliable parametrization has been performed previously.[33–37] We have not included any interaction designed to represent dipole → induced-dipole interactions or higher in-

duced-multiple interactions; however, these interactions have been calculated to be <5% of the total binding energy for carbazole·R[31] and aniline·R.[26] Three-body interactions have been estimated to be unimportant for the smaller clusters ($n \leq 4$), but their contribution may increase to ≈5% for larger clusters.[24,35] Both dipole-induced dipole and three-body interactions will be included in future calculations, even though the computational load increases by one order of magnitude. Although these contributions may not be decisive for the total binding energy and may even cancel to some degree, they are not distributed evenly over the whole cluster and can hence bias the structural characteristics of the clusters. We expect future developments of intermolecular potentials to lead to considerable improvements of this type of model.

Model calculations of this type have yielded excellent results for structural and energetic properties of aromatic molecule/rare-gas van der Waals complexes.[11,35,37] The minimum-energy structures of M·R van der Waals complexes with different M and $n = 1$ and 2 are very dependent on substrate size and shape; the results of model calculations and a classification of structural types have been discussed previously.[35] Argon solvent cluster structures have been previously calculated for tetracene·Ar_n (n = 1–3),[37] perylene·Ar_n,[24,29] and anthracene·Ar_n[59] by this or similar methods.

(ii) Molecular Dynamics Simulations. Minimum-energy (ME) and higher energy isomer structures were determined by molecular dynamics simulations, using the potentials described in (i). Simulated slow cooling, annealing, and quenching techniques were used to determine global minima (ME structures) and local minima (isomers) of the intermolecular potential energy hypersurface. The Newtonian equations of motion were solved by using the predictor–corrector integrating scheme suggested by Rahman,[53] the carbazole substrate being space fixed in the (x, y) plane. Varying the time steps from 5×10^{-15} to 5×10^{-14} s had no influence on the resulting structures.

(iii) Monte Carlo Simulations. To obtain equilibrium as well as stochastic "dynamic" properties of the clusters, Monte Carlo simulations were performed in the canonical (constant N, V, T) ensemble.[54,55] The system is treated as a collection of mass points interacting through the interatomic potentials described in (i). The canonical ensemble is advantageous for the present application, since the cluster vibrational temperature seems to be fairly well defined in our experiments. More details are given in section 3.3; concerning the use of Monte Carlo methods to obtain stochastic dynamical information, see ref 55.

3. Spectra, Structures, and Dynamics of Solute–Solvent Clusters

The electronic spectra of carbazole·Ar_n clusters are highly size dependent and exhibit highly characteristic band positions and band shapes. We will subdivide the discussion according to cluster sizes (small n = 1–8), medium (n = 8–20), large (n = 20–40)) and shape (two dimensional, three dimensional). Following presentation of the R2PI spectra, a number of the salient spectral features will be discussed and very briefly interpreted. A fuller discussion of the structural, dynamic, and energetic aspects of rare-gas solvent clusters will then be given and correlations to the observed spectral structure will be made.

3.1. Electronic Absorption Spectra: n = 1–8

The R2PI spectra covering the $S_1 \leftarrow S_0$ electronic origin region of the clusters with n = 1–8 are shown in Figure 2. The most important features are as follows:

(1) The solvent clusters with n = 1–3 exhibit sharp electronic origins, which are accompanied by sharp and discrete low-frequency intermolecular vibrational bands. The latter correspond to intermolecular motions of the cluster relative to the carbazole molecule, both parallel and perpendicular to the substrate surface. The observation of single, intense 0_0^0 bands implies the existence of unique and geometrically rigid cluster structures for n = 1–3. The observation of well-defined narrow solute–solvent vibrations also supports the notion that the solvent clusters are structurally rigid.

(2) For $n = 4$, a sharp electronic origin and intermolecular vibrational excitations similar to those of the smaller clusters are observed. These are, however, superimposed on a broad, structureless band, whose mean frequency coincides approximately with that of the 0_0^0 band. This broad feature is qualitatively very different from the hot-band or sequence-band structure as observed for, e.g., the $n = 3$ cluster, which is at a similar vibrational temperature (see below). The diffuse character implies that a second subpopulation of n = 4 clusters exists, which have a (quasi)continuous eigenvalue spectrum. This is strongly supported by the fact that the sharp:broad band integrated intensities vary from 2:1 to 1.2:1, depending on the cooling conditions achieved in the supersonic expansions. The MC simulations presented below show that the solvent clusters with $n \geq 4$ exhibit order–disorder transitions already at low internal temperatures (in the range T = 14–18 K); the resulting frequency spectrum of the two-dimensional fluxional clusters is expected to be quasi-continuous, in qualitative agreement with the observed band shape.

(3) Solvent clusters with $n = 5$ and 6 also show discrete, sharp peaks and broad, diffuse bands simultaneously (Figure 2). The intensity of the broad bands increases relative to that of the sharp bands on going from n = 4–6. The relative ratio of sharp:broad features can again be changed within certain limits by changing expansion conditions. These observations suggest that rigid/solidlike and disordered/fluxional structures coexist in this size range and that the rigid:fluxional population ratio depends on cluster size and temperature.

(4) For $n = 7$ the sharp bands vanish almost completely (although the four weak and sharp peaks on top of the broad feature are reproducible). For $n \geq 8$ no sharp structure remains (Figure 2). The disappearance of spectral fine structure in this cluster size range indicates that the trend toward a disordered/liquidlike state, which started at $n = 4$, is complete.

(5) For $n = 4$ and 5, the average frequencies of the broad bands coincide closely with the electronic origins; For $n = 6$, on the other hand, there is a *bifurcation of spectral shifts*: the broad band is shifted about 20 cm^{-1} further to the red than the sharp electronic origin. These spectral differences reflect changes in the atom density distribution function of the solvent cluster over

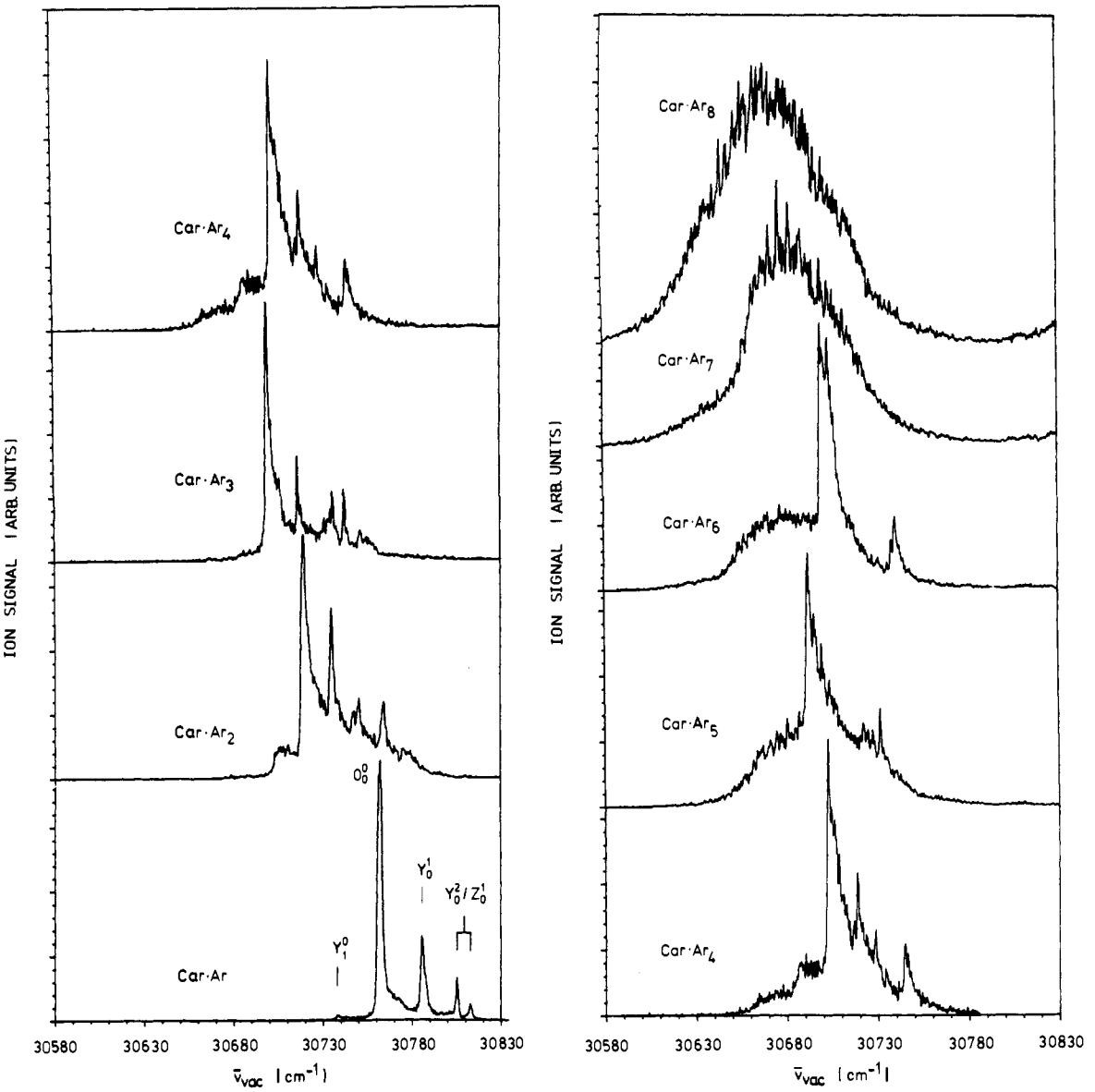

Figure 2. Resonant two-photon ionization spectra of carbazole·Ar_n with (a) n = 1–4 (left) and (b) n = 4–8 (right) covering the region of the electronic origin bands.

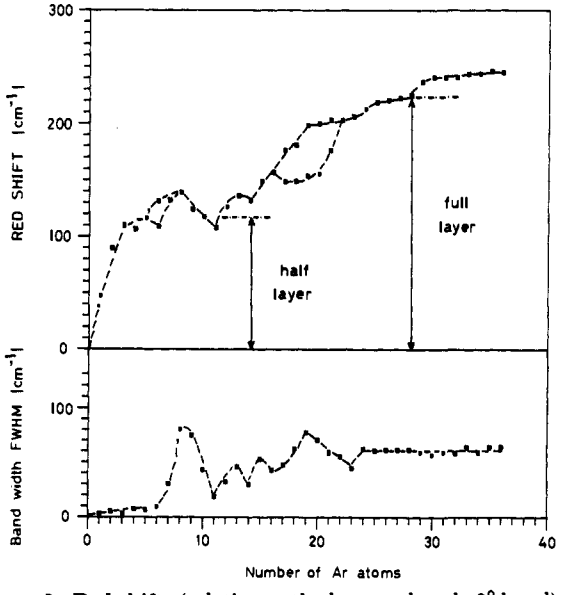

Figure 3. Red shifts (relative to the bare carbazole 0_0^0 band) and bandwidths (FWHM) of the electronic origin bands of carbazole·Ar_n clusters with n = 1–36.

the molecular surface (see section 3.3). In particular, we show below that the disordered/fluxional clusters may exhibit side-crossing transitions, i.e., partial or part-time atom transfer to the second side of the molecule.

(6) The shifts of the electronic origins relative to the bare carbazole electronic origin, $\delta\nu$, are to the red, implying that the excited-state binding energies ($D_0(S_1)$) are larger than the ground-state binding energies, since $\delta\nu = D_0(S_0) - D_0(S_1)$. The evolution of the red shifts as a function of n, $\delta\nu(n)$, in the size range n = 1–35 is shown in Figure 3. One notes that there is a rapid initial increase in $\delta\nu(n)$ for n = 1–3, followed by a plateau region for n = 3–14, over which the red shifts vary within a comparatively narrow range $110 < \delta\nu < 140$ cm^{-1}. The application of several well-established red-shift additivity rules[11,21,24,29] indicates that in the n = 1–14 size range the solvent cluster growth starts and continues on the same side of the carbazole molecule, yielding (n/0)-type solvent clusters, i.e., with n and 0 atoms adsorbed on the top/bottom sides of the substrate. Alternative hypotheses for cluster growth, e.g.,

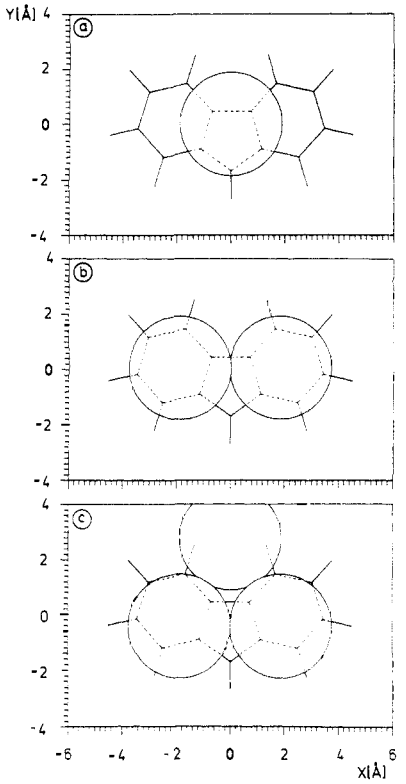

Figure 4. Minimum-energy structures of carbazole·Ar_n clusters with n = 1–3 calculated by molecular dynamics minimization.

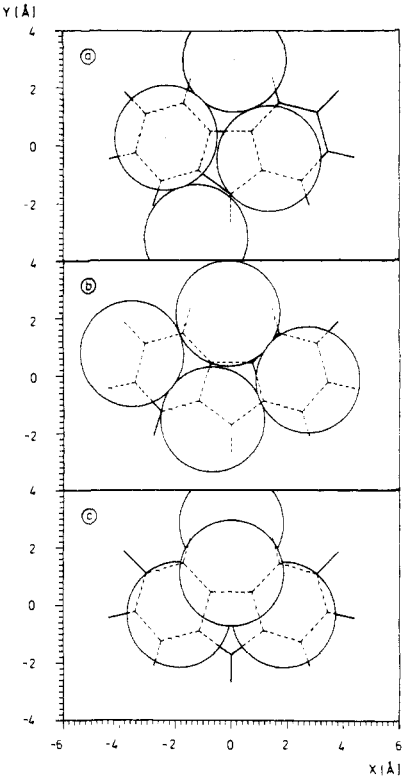

Figure 5. Calculated carbazole·Ar_4 cluster structures: (a) minimum-energy structure, binding energy V_4 = −2032 cm^{-1}; (b) isomer with 12-cm^{-1} smaller binding energy; (c) double-layer isomer, 147-cm^{-1} smaller binding energy. Several other stable isomers found by MD minimization are not shown.

adsorption on alternating sides of the substrate, are inconsistent with the observed red-shift pattern.[32,36]

(7) The rapid saturation of the red shift after n = 3–6, together with the calculations of cluster geometry described below, indicates that for atoms adsorbed over the central part of the substrate (the carbon ring framework) there is a differential red shift of 40–45 cm^{-1} per added argon atom, but essentially zero red shifts or even small blue shifts arise from solvent atoms adsorbed over the peripheral hydrogen atoms.

(8) From n = 14 on, a second rapid increase in red shifts is evident up to n = 19, followed by a second plateau in the size range n = 19–28. This development is qualitatively similar to that for n = 1–14. We also note that the total red shift for n = 1–14 is approximately equal to the total red shift for n = 14–28, being $\delta\nu \approx -115$ cm^{-1}.

3.2. Quasi-Two-Dimensional Cluster Structures

For n = 1–5, the calculated ME structures are all "same-sided" with the solvent cluster forming a contiguous two-dimensionally close-packed structure above the central part of one side of the substrate. Only one energetically low-lying structure was found for n = 1–3; these are shown in Figure 4. These ME structures all exhibit a plane of symmetry, i.e., the point group symmetry of the complex is C_s. This reflects an orientational ordering of the adcluster by the carbazole molecule, which results from close structural commensurability of the adcluster and substrate. This phenomenon is conceptually similar to that of surface registry of rare-gas monolayers on the (0001) basal plane of graphite.[60-66]

The ME structures obtained for the n = 4 cluster, which are shown in Figure 5, exemplify three new features:

(i) There are two cluster structures (Figure 5a,b) that are energetically very close. The structures differ only by a rotation of the Ar_4 rhomb relative to the carbazole substrate by ~90° (Figure 5a,b). Their binding energies are V = −2032 cm^{-1} and V = −2020 cm^{-1}, respectively, differing by only 12 cm^{-1}. The existence of energetically low-lying solvatomer structures implies the possibility of isomerization already at low internal temperatures, as will be verified in the MC simulation.

(ii) Neither of the ME structures exhibits symmetry.

(iii) The MD minimization also produced two locally stable solvatomers with bilayer cluster structures; the more stable solvatomer is shown in Figure 5c. However, the binding energies of these bilayer solvent clusters are less than that of the ME structure by ≈147 and ≈196 cm^{-1}, respectively.

The ME structures of the n = 5–7 clusters are shown in Figure 6. These larger clusters exhibit many distinct isomers: the number of isomers found within 150 cm^{-1} of the absolute energy minimum (not counting enantiomers) is 8, 17, and 6 for n = 5, 6, and 7, respectively. All n = 6 isomers exhibit an obvious atom "vacancy"; this results in a low barrier to intracluster diffusion-type motions. The minimum-energy structure for n = 7 is, however, predicted to be differentially quite stable, the next highest isomer having 136 cm^{-1} less binding energy.

The prediction of many energetically low-lying structural isomers of the larger clusters is suggestive of a purely heterogeneous spectral broadening mechanism for the observed diffuse spectral bands. However, the 0 K structure calculations predict heterogeneous broadening to be moderate for n = 4, important for n = 5 and 6, but unimportant for n = 7, which is in disagreement with the experimental observations.

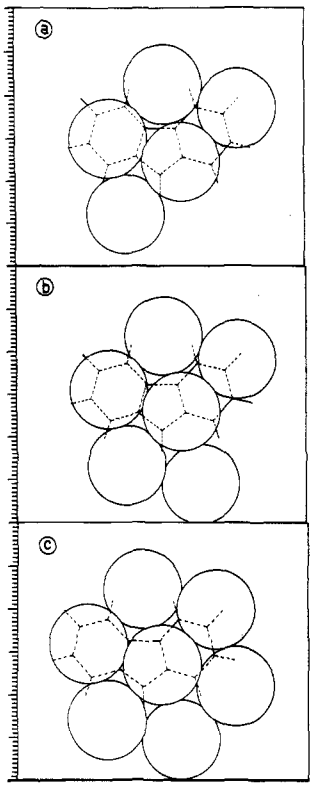

Figure 6. Calculated same-sided minimum-energy structures of carbazole·Ar_n with n = 5–7.

Summarizing the evolution of calculated solvent cluster structures for n = 1–7, we note the following characteristic features:

(*a*) *Quasi-two-dimensionality*: The dominant carbazole–cluster interactions are perpendicular to the molecular surface, so the minimum-energy cluster geometries are nearly flat, monolayer, raftlike structures. Bilayer structures found for $n \geq 4$ correspond only to local minima, with binding energies typically 5–15% less than those of the monolayer structures. We note, however, that the binding energies of bilayer structures approach those of the monolayer structures as size increases (see Figure 7 and below).

(*b*) *Two-dimensionally closest-packed structures* are found for all single-layer cluster structures. This reflects the strength of the Ar–Ar cohesive forces, which are substantially larger than the carbazole–Ar_n force components *parallel* to the molecular plane. The force constants for the carbazole–Ar intermolecular vibrations parallel to the substrate plane are of the order of f = 0.05–0.1 N m^{-1}, whereas the force constants for the Ar–Ar interaction are typically $f_{Ar-Ar} \sim 0.8$ N m^{-1}.

(*c*) *Orientational ordering* of the adcluster relative to the aromatic molecule occurs only for the smallest clusters (n = 1–3), which have overall C_s symmetry. For the larger clusters, nonsymmetric (chiral) structures are the rule.

(*d*) *Many energetically close-lying isomers* exist for n = 4–7, which differ only by rotations or translations of the adcluster relative to the carbazole surface. Hence the clusters are expected to isomerize by surface rotations/translations even at low internal temperatures (see below).

(*e*) *Vacancies and excess atoms*: The Ar_7 cluster is a two-dimensionally closed-shell structure (see Figure 6), and the n = 6 and 8 clusters exhibit an atom

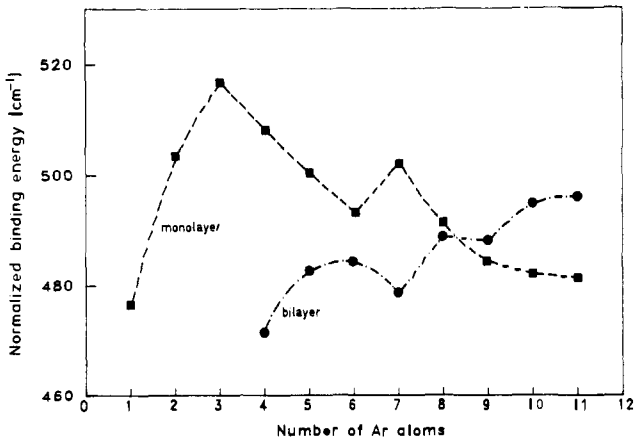

Figure 7. Calculated normalized binding energies, V_n/n, of monolayer (■) and bilayer (●) carbazole·Ar_n clusters with n = 1–11.

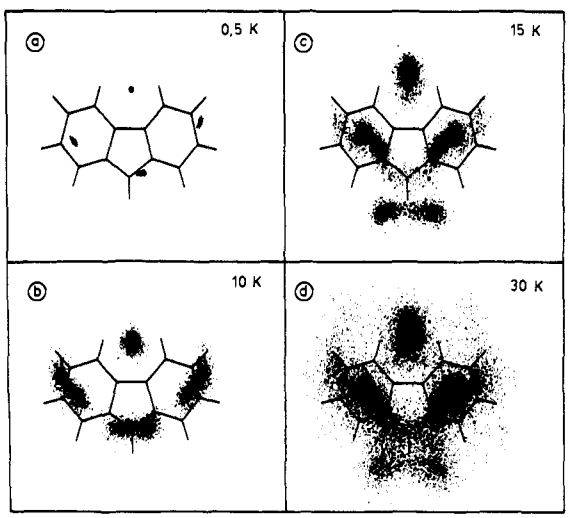

Figure 8. Solvent atom spatial probability density distributions calculated by the Monte Carlo method for carbazole·Ar_4 at (a) T = 0.5 K, (b) 10 K, (c) 15 K, and (d) 30 K.

"vacancy" and an "excess" atom, respectively (see Figures 7 and 13). This results in lower barriers to isomerization, and an increased atom mobility, as will be seen below.

3.3. Order–Disorder Transitions in Two Dimensions

A description of rare-gas solvent clusters at any but the lowest internal temperatures cannot proceed from a static, rigid-molecule point of view. The main reason for this is the existence of a very large number of minima in the potential energy hypersurface, usually separated by low barriers, which lead to facile interconversion between different isomers and the appearance of nearly free surface translation/rotation even at low internal energies. The problem of describing these finite-temperature structural distributions and interconversions was investigated by Monte Carlo simulations. Since the present discussion focuses mainly on the structural transitions of the solvent clusters, we have evaluated (a) the spatial probability density distributions ρ of the Ar atoms relative to the carbazole substrate frame, $\rho_i = \rho(\{x_i,y_i,z_i\};T)$, with i = 1...n (see, e.g., Figure 8), (b) the root-mean-square (RMS) displacements of the atomic positions of each Ar atom, σ_i (i = 1...n), in a carbazole-fixed coordinate system

$$\sigma_i = (\langle r_i^2\rangle - \langle r_i\rangle^2)^{1/2} = \{\sum(r_i - \langle r_i\rangle)^2/N\}^{1/2}$$

which characterizes the *rigidity of the Ar cluster relative to the substrate frame* (we note that the mean square displacement σ_i^2 can be experimentally determined for solids through the Debye–Waller factor, and for liquids through the diffusion coefficient), and (c) the normalized RMS Ar–Ar bond length fluctuation

$$\delta_{ij} = \{\langle d_{ij}^2\rangle - \langle d_{ij}\rangle^2\}^{1/2}/\langle d_{ij}\rangle$$

between Ar atoms i and j, which characterizes the *internal rigidity of the solvent cluster*. We note that, for molecules or clusters, δ can be determined by gas-phase electron diffraction.

Examination of these structural order parameters shows an astonishing series of order–disorder transitions of the Ar_n solvent clusters. We have so far found *seven* qualitatively different order–disorder transitions, four of which are important for the understanding of the various spectral features. In order of rising temperature, these are (1) surface isomerization/racemization transitions, (2) cluster rigid–fluxional transitions, (3) surface-decoupling transitions, (4) second-layer atom promotion, (5) atom side-crossing transitions, (6) wetting–nonwetting transitions [a combination of (4) and (5)], and (7) cluster melting transitions. The first three transition types are quasi two-dimensional (2-D) transitions and are of prime importance for the cluster size range n = 1–7; they will be illustrated with the n = 4 cluster, which is the smallest system exhibiting all of the 2-D transition types. The transitions (3)–(5) are three-dimensional transitions.

All structural changes described in this section and further below are, strictly speaking, isomerizations, since they occur in finite systems and do not fulfil the statistical mechanical criteria for true phase transitions. However, since most of these structural transitions involve large, collective coordinate changes, random diffusion of atoms throughout the accessible configuration space, and (near) complete permutation of the solvent atoms, they appear to be finite-system analogues of bulk order–disorder or phase transitions, and we will use the term "transition" accordingly.

3.3.1. Isomerization and Racemization

The disorder transitions that occur at the lowest temperatures involve only moderate changes of the solvent atom coordinates and are well described as *isomerizations* or *racemizations*.

At the racemization and isomerization transitions, interconversion takes place between different enantiomers (for n = 4–7) or isomers (for n = 6 and 8). Figure 8a,b shows a *racemization* transition as manifested by the spatial distributions for one isomer of the n = 4 cluster. The transition converts the nonsymmetric (chiral) cluster structure (Figure 8a) to the time-averaged C_s symmetric form (Figure 8b). The large-amplitude motion that interconverts the enantiomers is a hindered rotation, in which the rotation axis passes through the "pivot" atom lying in on the σ_v symmetry plane.

Racemization of these quasi-two-dimensional clusters is characterized by steplike increases of several (but usually not all) RMS atomic displacements. Figure 9a,b shows the temperature dependence of the σ_i values for the n = 4 cluster: $\sigma_{1,3,4}$ increase in a sharp steplike

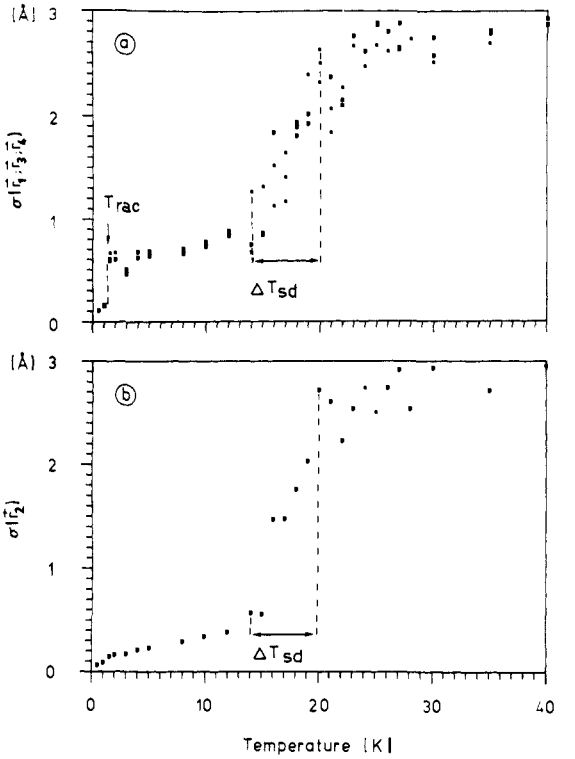

Figure 9. Temperature dependence of the RMS atomic displacements σ_i of carbazole·Ar_4 for (a) the three "lower" atoms in Figure 8a,b, and (b) the "top" atom in Figure 8a,b. Note that the racemization transition at T_{rac} = 1.5 K is evident in (a), but not in (b), whereas the surface-decoupling transition, which occurs over the range ΔT_{sd} = 14 to 19 K is clearly observed in both (a) and (b), i.e., for all four atoms in the cluster.

fashion from ~0.15 to ~0.7 Å. We denote this characteristic temperature as the *racemization temperature* T_{rac} = 1.5 K. By contrast, the pivot atom shows only a slow monotonic increase in σ_2 up to T = 14 K. Since the transition interconverts mirror symmetric forms, the spectroscopic changes accompanying the transition should be barely observable.

The *isomerization* transitions typically involve motions of a single atom within the cluster and, so far, have been found for n = 6 and 8. These clusters have many energetically close-lying isomers that differ only by the position of the vacancy or excess atom, respectively. Isomerization transitions hence involve motion of the vacancy or excess atom.

3.3.2. Rigid–Fluxional Transitions

At the rigid–fluxional transition temperatures, the solvent clusters undergo structural changes that involve some, but not all, *intracluster* Ar–Ar bonds. The transitions are characterized by sharp steplike increases in the RMS bond length fluctuations δ_{ij} of the corresponding bonds between atoms i and j. An example is again provided by the Car·Ar_4 cluster: at T = 14 K, the "diagonal" bonds of the rhomb-shaped Ar_4 cluster soften and simultaneously contract or expand in a concerted motion. This movement interconverts the ME structure (Figure 5a) and the low-energy isomer (Figure 5b). This motion is also equivalent to a pseudorotation of the cluster relative to the substrate by ≈90°. The effect of pseudorotation is clearly seen in the probability density distributions shown in Figure 8b,c: the former corresponds to a thermally broadened structure as shown in Figure 5b, while the latter corresponds to a

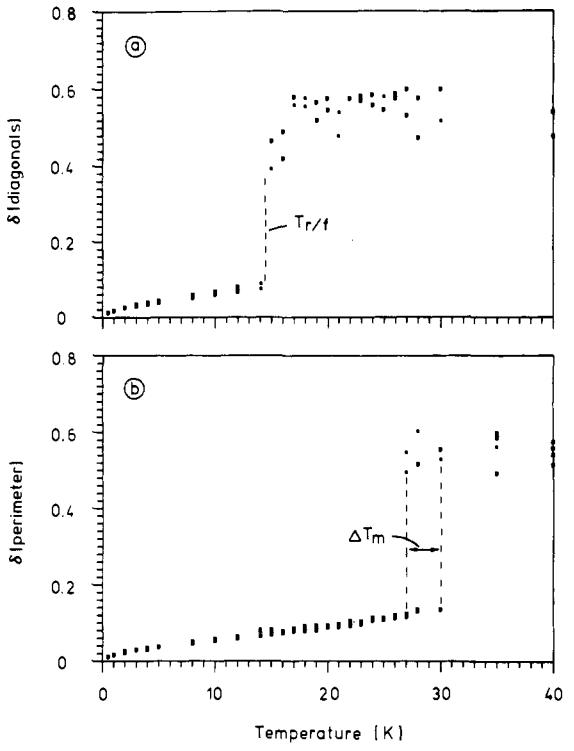

Figure 10. Temperature dependence of the RMS bond length fluctuations δ_{ij} for carbazole·Ar_4: (a) for the diagonal bonds d_{13} and d_{24}; (b) for the perimeter bonds d_{12}, d_{23}, d_{34}, and d_{14}. The rigid–fluxional transition, which corresponds to a fluctuation of the Ar_4 diagonal bonds only, is steplike and occurs at $T_{r/f}$ = 14.5 K (a). The intrinsic melting process of the adcluster, which permutes Ar atoms within the cluster, occurs over a finite-width melting range ΔT_m = 27–30 K (b).

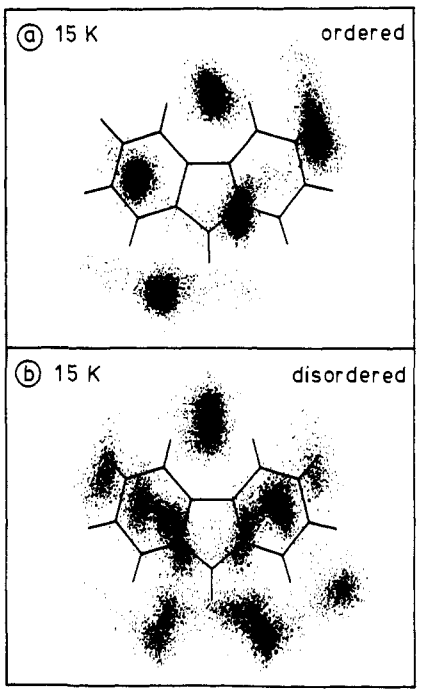

Figure 11. Probability density distributions for carbazole·Ar_5 [$\rho(x,y);T$=15 K)] obtained by MC simulations of 10^6 steps. (a) A simulation is shown that resulted exclusively in a rigid or solidlike structure. (b) A different run *at the same temperature* shows that surface decoupling has occurred, in which the orientation of the adcluster relative to the substrate has become fluxional.

superposition of the structures depicted in Figure 5a,b, which interconvert by pseudorotation (and also by rigid-body rotation due to the surface-decoupling transition; see below).

Figure 10a shows that the rigid–fluxional transition is characterized by a very sharp increase of the diagonal bond length fluctuations $\delta_{1,3}$ and $\delta_{2,4}$ at $T_{r/f}$ = 14.5 ± 0.5 K from ≈8% to ≈50%! Note that the RMS bond length fluctuations of the four perimeter Ar–Ar bonds, which are shown in Figure 10b, show no change at this temperature, indicating that *the cluster perimeter is not affected by the rigid–fluxional transition.* The transition occurring at $T \geq 27$ K is related to intracluster melting (see section 3.3.4).

3.3.3. Surface-Decoupling Transitions

In the surface-decoupling transitions, the adcluster loses orientational ordering relative to the host molecule and becomes free to undergo large-amplitude, very-low-frequency rotational/translational motions or hops with respect to the substrate. Since the barriers hindering these motions are generally of comparable but unequal height, the surface-decoupling transitions, as measured by the increases in σ_i, are sluggish and take place over a fairly wide range ($\Delta T \sim$ 3–5 K). At the lower end of the transition range, some of the barriers are crossed infrequently, while at the upper end of the range, all of the barriers are crossed frequently. Thus the relative concentrations of surface-decoupled/surface-locked clusters and the frequency of large-amplitude hopping both increase over this range. We point out that although the cluster orientation relative to the substrate is completely fluxional, the solvent cluster itself is *not* liquidlike up to 25–30 K, since the large majority of the intracluster bonds remain "stiff", with $\delta_{ij} < 10\%$.

Surface decoupling is characterized by increases in *all* of the σ_i values from $\sigma_i \leq 0.6$ Å at the lower end to $\sigma_i \geq 1.8$ Å at the upper end of the transition range. The transition ranges are 14–19 K (n = 4), 16–19 K (n = 5), and 18–21 K (n = 6, 7). Figure 8b,c exemplifies the effects of the combined rigid–fluxional and surface-decoupling transitions in carbazole·Ar_4.

Near the lower end of the transition range, the simulations frequently show that the solvent clusters are either substrate locked or decoupled for large fractions of the Markov chain (up to 10^6 steps). An example of this behavior is shown for the n = 5 cluster in Figure 11: for MC runs of 10^6 steps, the cluster remains in either a substrate-locked (Figure 11a) or substrate-decoupled phase (Figure 11b), which differ completely in the distribution of solvent atoms.

Potential Energy Distributions. The difference between substrate-locked and substrate-decoupled clusters is also evident from the potential energy distributions corresponding to Figure 11, which are shown in Figure 12a,b: the substrate-locked or ordered phase clearly exhibits a lower average potential energy than the substrate-decoupled cluster. These characteristic differences in the potential energy distributions are quite analogous to those between bulk solid and liquid phases. At the melting point, the average potential energy of a bulk solid is lower than that of the corresponding bulk liquid, i.e., $\langle V \rangle_{solid} < \langle V \rangle_{liquid}$. Also shown in Figure 12 is a longer run of 2×10^6 steps which encompasses both "phases" of the cluster (Figure 12c). This behavior is typical for all solvent clusters with n = 4–7 over the

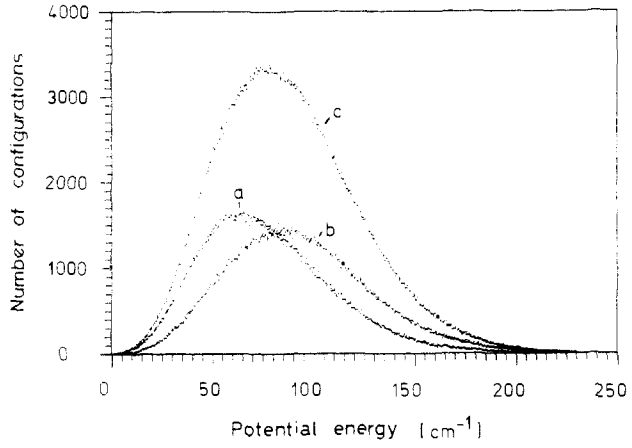

Figure 12. Potential energy probability density distributions for carbazole·Ar_5: (a) and (b) correspond to the MC runs shown in Figure 11a,b; (c) is the potential energy distribution obtained for a separate run of 2×10^6 steps that encompasses both rigid and fluxional forms of the Ar_5 adcluster.

surface-decoupling transition ranges. It has been reported previously by Berry and co-workers to occur for "melting" transitions in MD and MC simulations of some pure Ar_n clusters.[46]

3.3.4. Cluster Melting

The intrinsic melting process of the solvent clusters is characterized by increases of *all* RMS bond length fluctuations from $\delta_{ij} < 10\%$ to $\delta_{ij} \geq 40\%$. This is in excellent agreement with the Sutherland–Lindemann criterion for bulk melting, which states that a solid melts when the thermal RMS vibrational amplitude of the constituent atoms (molecules) increases above 10%. The melting transition of a bulk crystalline material shows a sharp melting point, which is accompanied by marked changes in density, heat capacity, etc. This is due to the difference in ordering between the solid and liquid phases, which is reflected in the difference in entropies of the two phases, and can be quantified by an order parameter. Cluster "melting" transitions take place over a *temperature range*, for two reasons: (1) due to the generally low symmetry of the clusters, the entropies of the solidlike and liquidlike forms are very similar, and melting transitions become similar to glass → liquid transitions (viz., Berry's concept of "slush" in cluster melting[46]). In the present case, the order parameters σ_i and δ_{ij} provide convenient and sensitive microscopic indicators of the occurrence of transitions, while other properties (e.g., specific heats) do not.[68] (2) For first-order transitions such as melting, the finite size of the system (n particles) leads to a smearing of the melting temperature T_m over a finite range ΔT_m, $\Delta T_m/T_m \approx k_B/n\Delta S_m$, where k_B is the Boltzmann constant and ΔS_m is the latent entropy of the corresponding bulk system.[69]

As in the surface-decoupling transitions, the simulations reveal the coexistence of solidlike and liquidlike cluster phases at the same temperature, with a finite-width melting range of 3–5 K. An example is given in Figure 10b: at 27 K, the δ values of the perimeter bonds increase from <10% to 40–60%, indicating rupture of perimeter bonds and thus complete disordering or "melting" of the adcluster. Note that the δ_{ij}'s show hysteresis-type loops as a function of temperature over the melting range T_m = 27–30 K. Figure 8c,d allows

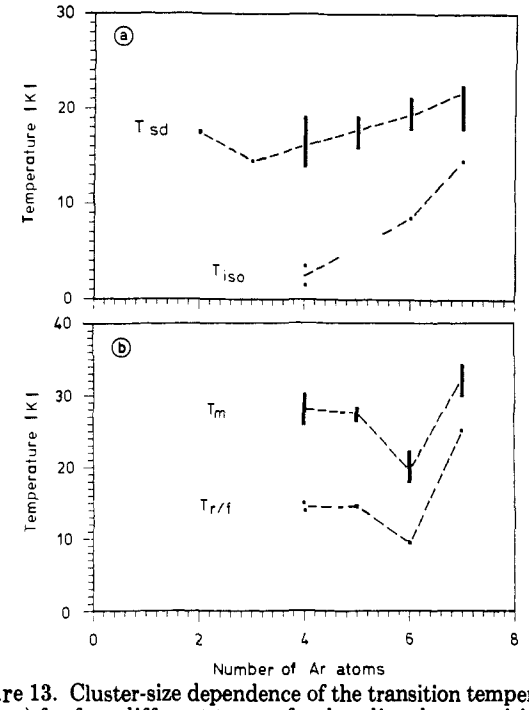

Figure 13. Cluster-size dependence of the transition temperature (ranges) for four different types of order–disorder transitions in quasi-two-dimensional carbazole·Ar_n clusters (n = 4–7). T_{sd} indicates the surface-decoupling transition temperature range; T_{iso}, the isomerization or racemization transition temperature; T_m, the intracluster melting temperature range; and $T_{r/f}$, the intracluster rigid–fluxional transition temperature.

direct visualization of the cluster melting process, where Figure 8c represents the system within the surface melting temperature range, but below the cluster intrinsic melting range.

The transition temperatures or temperature ranges are shown in Figure 13 for the quasi-2-D clusters with n = 4–7. The sequence of order–disorder transitions with rising temperature is usually the following: isomerization/racemization < rigid–fluxional $\lesssim$ surface decoupling < cluster melting. The trends of transition temperatures with increasing n depend on the type of transition: the surface-decoupling temperatures show a slow increase with increasing cluster size and comparatively little fluctuation. On the other hand, the racemization/isomerization transition temperatures are different for each cluster. This reflects the "molecular" nature of these transitions; the transition temperature depends on the lowest potential energy barrier that can be surmounted.

Turning to the intracluster-type transitions, we note the exceptionally low transition temperatures of the rigid–fluxional and melting transitions of the n = 6 cluster. These are both markedly lower than those of n = 5 and 7. This is obviously related to the atom vacancy (see Figure 6b); as in bulk solids, where the existence of vacancies increases the diffusion constant by orders of magnitude, the atom vacancy is seen to promote intracluster "diffusion" and disorder. A compilation and comparison of transition characteristic are also given in Table I.

3.4. Spectroscopic Effects of Two-Dimensional Order–Disorder Transitions

The electronic origin of the $S_1 \leftarrow S_0$ electronic transition (π–π^*) of the carbazole molecule is utilized as a

TABLE I. Order-Disorder Transitions of Carbazole•Ar_n Solvent Clusters

	cluster/substrate		intracluster	
	type	range, K	type	range, K
two-dimensional transitions	racemization / isomerization	1–15	rigid–fluxional	8–15
	surface decoupling	14–21		
three-dimensional transitions	side crossing	20–23	cluster melting	25–32
	wetting–nonwetting	20–38		

spectroscopic "probe". The transition is itself localized within the substrate, and the solvent environment is only a small perturbation. Here we outline the main factors influencing the position, width, and shape of the electronic origin band:

(*i*) *Static Structural Effects.*[10,33,36] The electronic origin transition frequency of the bare molecule, ν_0, is shifted by the microscopic solvent surrounding. For a given cluster size n, the interaction energies in both the ground and excited states, $V_n(S_0,S_1)$, depend on the instantaneous geometrical configuration of the solvent atoms relative to the substrate molecule and to each other, and hence the transition frequency for any given geometry is

$$\nu_0^i(n) = \nu_0 - V_n(S_0) + V_n(S_1)$$

Thus ν_0 is shifted to the blue or red, depending on the cluster structure and size, via the intermolecular interaction energies. At very low temperatures and small n, the spectral shift $\delta\nu(n)$ of the electronic origin reflects this change for the minimum-energy configuration. At nonzero temperatures, the distribution over many different static cluster structures results in a distribution of spectral shifts, resulting in inhomogeneous broadening.

(*ii*) *Order–Disorder Transitions.*[33,36] Isomerization transitions of the clusters result in a smearing-out of the spatial distributions of one or several adatoms. The rigid–fluxional and surface-decoupling transitions further expand the accessible region of configuration space and also increase the isomerization rates. As a result, the cluster may cover a *range* of structures within the time interval of the spectroscopic experiment, and *broadening* of the electronic transition will occur. Depending on the time scales of the structural change of the cluster and of the experiment, the broadening may be purely inhomogeneous (see (i) above), purely homogeneous, or a mixture of both.

(*iii*) *Electronic–Vibrational Couplings.*[10,33,36] Even for rigid clusters, the low-frequency carbazole ↔ Ar and Ar ↔ Ar intermolecular vibrational modes couple to the electronic transition. For the solidlike clusters at low internal energies, the vibrational level densities are low, and excitation of discrete levels is observed (e.g., for n = 1–6; see Figure 2): The Franck–Condon factors for the excitation of intermolecular modes are quite low, typically <0.1. For the larger clusters or at higher excitation levels, the vibrational level densities become high and a more appropriate description is that of electron–"phonon" coupling. By extrapolation from the small clusters and also from the spectra where phonon excitation is observed (n = 11, 14), we estimate that the Huang–Rhys factor is $S < 0.1$, i.e., that the limiting case of weak electron–phonon coupling prevails. In a fluxional/liquidlike cluster there is no clear distinction between diffusive-type motions of the solvent atoms responsible for isomerization and vibrational modes in which the solvent atoms move parallel to the substrate surface. The frequency spectrum is expected to be continuous and extend out to very low values.

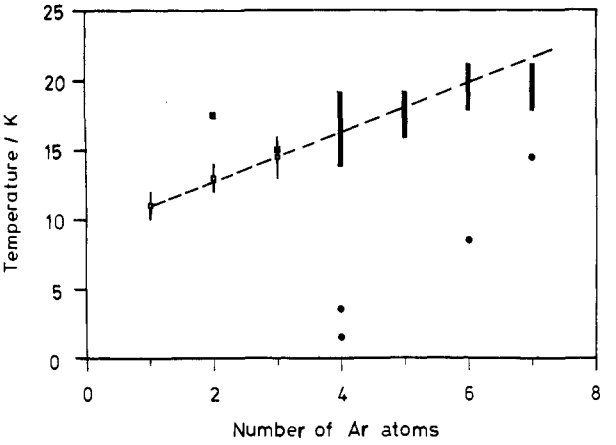

Figure 14. A comparison of calculated surface-decoupling transition temperatures for n = 1–7 (■ or vertical bars) with experimental vibrational temperatures for n = 1–3 (□) extrapolated to n = 7 (---). Also included are the calculated racemization or isomerization temperatures (●); the n = 5 cluster does not exhibit an isomerization transition.

We now return to a discussion of the characteristic features of the electronic origins in Figure 2a,b:

(*1*) *Intermolecular Vibrational Excitations.* The fine structure observed on both sides of the electronic origins of the n = 1–6 clusters corresponds to excitations of intermolecular carbazole–Ar_n vibrations in the S_1 state (to the blue of the origin) and in the S_0 state (weak hot bands on the red side of the origins). They can be interpreted as motions of the solvent cluster parallel to the carbazole surface (Y modes) and perpendicular to the carbazole surface (Z modes) and have been previously treated in detail.[32,35,36] The internal temperatures of the n = 1–3 clusters can be estimated by the ratio of the intensity of the Y_1^0 bands relative to the Y_0^1 bands, with the assumption that the FCF's are equal for both transitions.[33,34] Approximate vibrational temperatures are 11 ± 2 K (n = 1), 13 ± 2 K (n = 2), and 15 ± 3 K (n = 3). Extrapolating linearly to higher n, we estimate internal temperatures in the range T_{vib} = 16–22 K for n = 4–7. The observed and extrapolated vibrational temperatures for n = 1–7 are plotted in Figure 14.

For n = 2 and 3, the internal temperatures are below the surface-decoupling temperatures, which are sharp for these two clusters. This correlates well with the spectra in Figure 2, which show no evidence of fluxionality.

(*2*) *Broad Spectral Features.* The appearance of a broad band at n = 4 is interpreted as the spectroscopic manifestation of the onset of order–disorder transitions, specifically of the rigid–fluxional and surface-decoupling transitions, with transition temperatures of T = 14 K and T = 14–19 K, respectively. We estimate the tem-

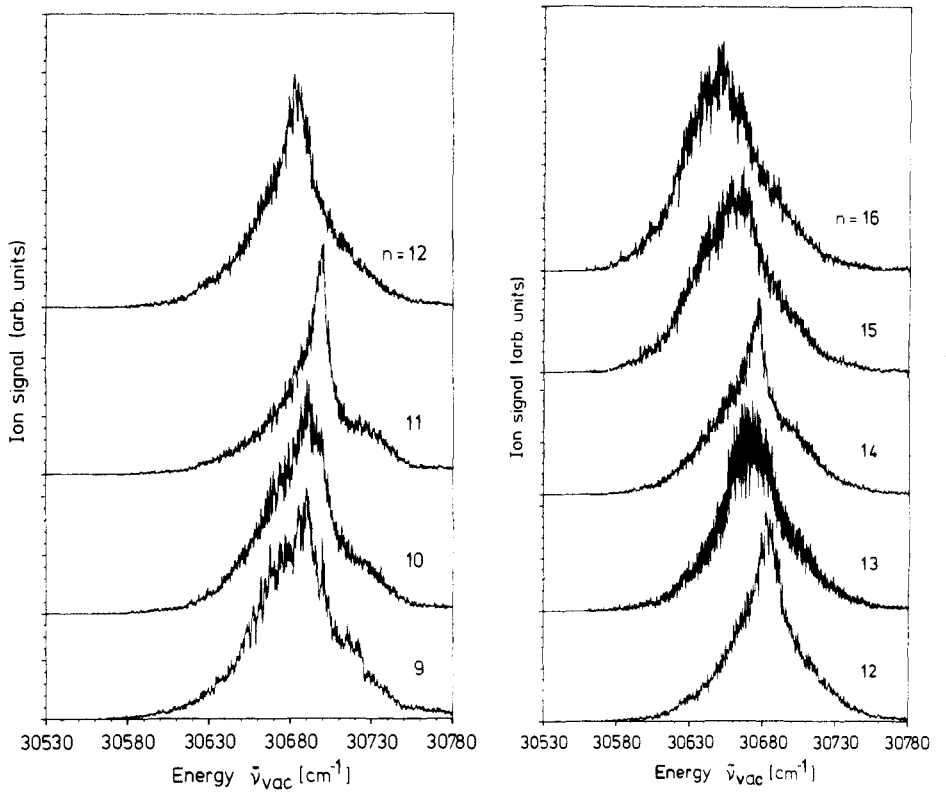

Figure 15. Resonant two-photon ionization spectra of the electronic origin regions of the carbazole·Ar$_n$ clusters with n = 9–16.

perature of the n = 4 cluster by linear extrapolation from n = 1–3 as T = 16 ± 3 K, which lies within the range of the surface-decoupling transition.

(3) *Simultaneity of Sharp and Broad Spectral Features.* The MC simulations indicate that for n = 4–7, the surface-decoupling transition takes place over a range of 3–6 K and that within this range, the cluster ensemble shows both rigid and fluxional behavior at a defined temperature. By linear extrapolation from n = 1–3, the internal temperatures of n = 4–6 are estimated to lie within, and for n = 7, at or slightly above, the upper limit of the surface-decoupling temperature range. The simultaneous appearance of sharp and broad features in the electronic spectra is thus believed to be the spectral signature for the coexistence of rigid and fluxional clusters over a limited range of temperatures and sizes.

(4) *Sharp:Broad Band Intensity Ratios.* For n = 4–7, the increase of the intensities of the broad features relative to the sharp features with increasing n is qualitatively clear from Figure 2b. This trend agrees with the simulations, which predict that the fraction of fluxional clusters rises with increasing temperature within the order–disorder transition range.

(5) *Disappearance of Sharp Bands.* The sharp spectral bands disappear almost completely for n = 7 and completely for n = 8, indicating that these solvent clusters have no rigid, surface-fixed geometries on the experimental time scale. The extrapolated temperatures for n = 7 and 8 are T = 21 ± 3 K and T = 23 ± 3 K, respectively, lying above the upper limit of the surface-decoupling temperature range.

To summarize, the spectral trends of Figure 2 can now be rationalized in a straightforward manner, as in Figure 14: solvent clusters that are below the surface-decoupling "freezing point" show sharp bands, clusters with internal temperatures falling inside the surface-decoupling temperature range exhibit both broad and sharp bands simultaneously, and clusters with internal temperatures above the surface-decoupling point or range show only a broad-band contour. Thus the general agreement between calculations and experiment provides strong support for the interpretation of the spectral band shapes in terms of surface-decoupling transitions with coexistence ranges of finite width.

3.5. Electronic Spectra of Half-Solvated Clusters: n = 8–20

The electronic origin bands of the larger Car·Ar$_n$ clusters with n = 9–16 are shown in Figure 15. Closer examination of the electronic origin bands and comparison with Figure 2b reveal three spectral trends that are related to the *first, second, and third moments* of the bands and that run essentially parallel:

(1) Starting at n = 6, the average red shifts of the electronic origins first increase, from $\delta\nu(6)$ = −105 cm^{-1} to a maximum red shift of $\delta\nu(8)$ = −145 cm^{-1}, and then decrease again to $\delta\nu(11)$ = −105 cm^{-1}. This pattern is repeated a second time for n = 11–14, with a maximum red shift at n = 13. The trends form two semicycles, which are shown in Figure 16a.

(2) The *widths*, $\Delta\nu$, of the electronic origin bands (FWHM) also increase from $\Delta\nu$ = 30 cm^{-1} at n = 6 to $\Delta\nu$ = 80 cm^{-1} at n = 8 and decrease again for n = 8–11. This pattern repeats for n = 11–14. There is a close resemblance to the red-shift pattern, as also shown in Figure 16a.

(3) Examination of the *skewness* of the electronic origins reveals that for n = 7 and 8 the bands are skewed toward the blue (higher transition frequencies), while for n = 9–11 they are skewed toward the red. The n = 12 origin is symmetric, n = 13 is positively skewed, and n = 14 is negatively skewed. Thus a further cor-

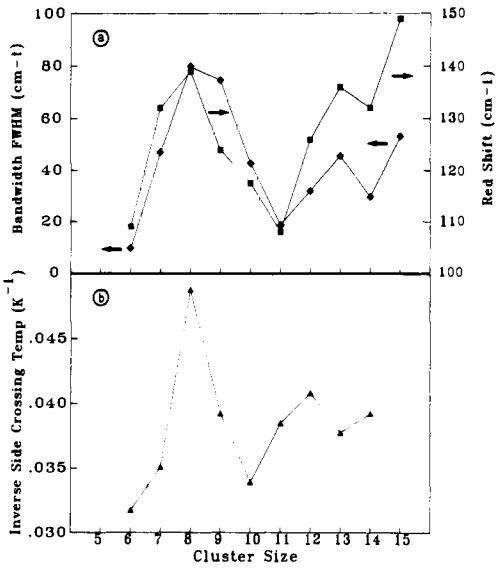

Figure 16. (a) Experimental bandwidths (♦) and red shifts (■) of the electronic origin bands of carbazole·Ar_n with n = 6–14; note the similarity of the trends for the two different experimental quantities. (b) Inverse side-crossing transition temperatures ($1/T_{SC}$) for n = 6–14 as calculated by MC simulations for single-sided mono- or bilayer structures (▲).

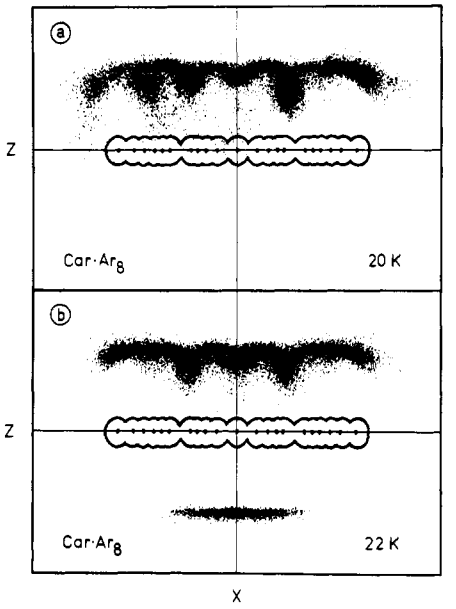

Figure 17. Side views in the x/z plane of the spatial probability density distributions of the carbazole·Ar_8 cluster in the temperature region over which atom side crossing is found: (a) at 20 K, below the side-crossing temperature; (b) at 22 K, above the side-crossing temperature.

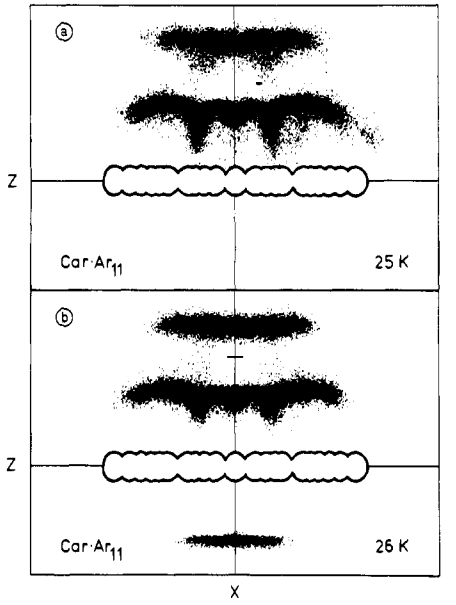

Figure 18. Views of the spatial distributions of the n = 11 cluster below and above the wetting–nonwetting transition: (a) at 25 K, below the transition; (b) at 26 K, above the transition.

relation of band shape with cluster size emerges: if the origin bands are shifted toward the red, they are skewed toward the blue, while if they shift toward the blue they are skewed toward the red.

Before discussing the detailed mechanism responsible for these features, we note that a very simple rationalization of these trends is possible, which rests on the observation that the red shift increases between n = 6 and 8 by 40 cm^{-1} but decreases between n = 8 and 11 by the same amount. This red increment is typically associated with adsorption of the first Ar atom on the substrate; i.e., $\delta\nu(1) \approx -40$ cm^{-1}. This suggests that the semicyclic red-shift trends are associated with the *solvation* (n = 6–8) and *desolvation* (n = 8–11) of the previously free or uncomplexed side of the carbazole molecule by (at least) one Ar atom.

The structure calculations as well as the MD and MC simulations indicate that these trends can be understood in terms of *three-dimensional* cluster structures and order–disorder transitions, which will be discussed in the following two sections.

3.6. Three-Dimensional Cluster Structures

The n = 7 monolayer cluster essentially covers one face of the carbazole solute. Further growth in the intermediate-size range n = 8–14 leads to a *trifurcation of structural types* that are energetically competitive:

(1) The first structural type consists of larger monolayer clusters of the type discussed above.

(2) The second structural type embodies sandwich-type clusters, in which the substrate is solvated on both sides. The clusters on each side are fairly independent of the other; i.e., the two adclusters are not connected by Ar–Ar interactions up to a size of $n \sim 14$. The experimental red shifts and band widths indicate that sandwich clusters become energetically favorable around n = 8.

(3) Finally, the third structural type consists of single-sided bilayer clusters. As noted above, the binding energies of bilayer cluster structures increase with increasing cluster size. Figure 7 shows the normalized binding energies V_{tot}/n of the lowest energy monolayer and bilayer structures for n = 1–11. Note that the calculated binding energies of the two structural types cross over at n = 8; clusters up to n = 7 are more stable as monolayers; the larger clusters prefer bilayer structures.

Figures 17 and 18 show examples of each structural type: carbazole·Ar_8 below 20 K is single-layer single-sided (Figure 17a); for $T \geq 21$ K, one or more atoms can cross to the second substrate side (Figure 17b). An example of the same-sided bilayer structures is shown in Figure 18a for carbazole·Ar_{11}. Multilayer structures can also occur: thus for carbazole·Ar_{12} one of the low-

energy structures is icosahedral with one atom removed from the outer shell.

3.7. Order–Disorder Transitions in Three Dimensions

At internal temperatures higher than $T \approx 20$ K, three types of order–disorder transitions occur that involve the third spatial dimension of freedom: *side-crossing* transitions, *second-layer promotion*, and *wetting–nonwetting* transitions. Among the microscopic mechanisms that drive 3-D order–disorder transitions are the following:

Geometrical effects: The average binding energy to the solute is largest on the nearly flat top and bottom surfaces, lower along the edges of the solute, and lowest at the "corners", i.e., inversely proportional to the convexity of the solute. Hence, solvation or wetting of different parts of the solute takes place in the same order.

Collective effects: Slight differences in solvent–solute binding energies tend to be magnified by the presence of other solvent atoms: preexisting solvent clusters encourage solvation of their immediate surroundings, since solute–solute binding interactions now also contribute to the total binding energy. Examples of this effect are the wetting–nonwetting transitions discussed below.

Entropic effects: The vibrational force constants are lower along the edges and corners of the solute and also for second-layer atoms. Hence, for cluster structures with less tightly bound atoms the lowest vibrational frequencies can be substantially lower than for close-packed single-layer structures. For the former, the vibrational partition function (and thus the $T\Delta S$ term) increases more rapidly with temperature, favoring the "looser" over the more compact structures, due to the entropy increase.

3.7.1. Side-Crossing Transitions

The crossing-over of an atom from the solvated side of the substrate molecule to the other, unsolvated, substrate side is energetically unfavorable for smaller clusters. Although the carbazole ↔ Ar interaction is smaller for the more peripheral Ar atoms, removal of a single atom from a preexisting solvent cluster entails the breaking of several R–R bonds. Thus, side-crossing occurs only at fairly high temperatures ($T \geq 30$ K) for solvent clusters with $n \leq 6$. However, for larger clusters the Ar interaction with the peripheral hydrogen atoms is low, so that the barrier to side-crossing rapidly decreases with increasing cluster size. All single-sided clusters exhibit a characteristic *side-crossing transition temperature*, the temperature above which side-crossing occurs for at least one atom. Figure 17 shows a view of the probability density distribution for the carbazole·Ar_8 cluster below and above the side-crossing transition at $T = 21$ K; the transfer of one atom to the lower side of the solute is clearly apparent.

3.7.2. Second-Layer Promotion

Promotion of one or more atoms from the first to the second solvent layer is the second important type of 3-D order–disorder transition. It is not observed in the MC simulations up to $n = 4$. In small clusters, atom promotion is energetically unfavorable, since the second-layer adatom is typically only bound by three solvent–solvent bonds. If, however, two or more atoms are promoted simultaneously due to fluctuations, the number of nearest-neighbor solvent–solvent contacts rises to 4–6 per adatom, providing sufficient self-stabilization of the second layer, as well as growth sites for additional second-layer atoms. Thus, for larger clusters this type of structural transition becomes rapidly favorable: for $n \geq 5$ the process occurs above $T_{2l} = 33$ K, and drops to the vicinity of $T_{2l} \approx 25$ K for larger clusters. The Ar atom density distribution normal to the carbazole substrate shows two well-defined peaks separated by a pronounced minimum region; the spatial separation allows the order parameters of each layer to be examined separately. The MC simulations for the size range $n = 8$–14 show that second-layer promotion and side-crossing transitions occur over similar temperature ranges and often occur in alternation during the same MC run. The relative importance of these two transitions depends sensitively on n in this size range.

3.7.3. Wetting–Nonwetting Transitions

The occurrence of wetting–nonwetting transitions on extended solid surfaces has its analogue in microscopic solvation: we find that solvation–desolvation or wetting–nonwetting transitions can occur in the size range $n = 8$–20 as a function of size and temperature. In the finite solvent systems, some parts of the solute molecule are preferentially solvated or wetted over others, and raising the temperature can result in a more even solvent distribution.

In the intermediate-size clusters, the simulations reveal several different kinds of wetting–nonwetting transitions. One example is shown in Figure 18: the $n = 11$ solvent cluster is single-sided bilayer up to 25 K. Above that temperature, one or more atoms are successively transferred from the outer solvent layer via the inner layer on the top side to the lower side of the solute (Figure 18b). This results in an increase of the solvated or wetted area of the solute, i.e., a nonwetting–wetting transition.

A second type of transition involves wetting of the sides of the solute: for sandwich-type clusters at temperatures $T \leq 25$ K, only the top and bottom surfaces of the solute are solvated, while the sides are completely unsolvated. In the temperature range $25 < T < 32$ K, atom exchange between the top and bottom layers becomes frequent, the predominant exchange pathways being two "corridors" on each side of the N–H group. While the "front" edge of the solute thus becomes partially solvated, the back edge remains completely unsolvated. Finally, above ≈33–35 K, solvent atom exchange also occurs via the back side, leading to partial wetting of both the front and back solute edges. Note, however, that the left and right edges of the solute are still far from being wetted.

A third type of wetting–nonwetting transition is the formation of a *second solvent layer* above the first layer, at temperatures higher than $T = 32$ K. This amounts to a combination of second-layer promotion with reverse side-crossing transitions: since the total number of solvent atoms is conserved, the two inner layers must lose population density to the newly formed outer solvent layer. This amounts to partial *desolvation* in favor of formation of a bilayer solvent "droplet", i.e.,

a wetting–nonwetting transition.

3.8. Spectroscopic Effects of Three-Dimensional Order–Disorder Transitions

In the cluster size range n = 8–14, the occurrence of three different types of cluster structures and the added dimensionality of the order–disorder transitions lead to large variations of the red shifts, bandwidths, and band shapes of the electronic origins, as pointed out in section 3.5. The degree of structural inhomogeneity and the order–disorder transitions that interconvert between the different structural types are the main two factors controlling the band shapes and bandwidths.

Structural Effects. The spectral red shifts are essentially determined by the (average) number of Ar atoms that are adsorbed above the aromatic framework within the C-atom perimeter, while peripherally bound Ar atoms, which are located near hydrogen atoms, contribute very little to the shifts. Hence cluster growth by monolayer extension leads to little additional red shifts. By contrast, in bilayer-type structures the contact or wetted area of the solute is *decreased* relative to the monolayer case, leading to differential *blue* shifts. Finally, in the sandwich-type cluster structures, the additional coverage of the central area of the second side of the solute leads to differential *red* shifts, compared to the corresponding single-sided monolayer-type structures.

For n = 8 the binding energies of all three structure types are comparable and expected to occur with similar probabilities. The side-exchange temperature is very low, T = 21 K, and at the estimated experimental temperature T_{exp} = 23 ± 3 K, atom exchange between the two sides is possible. The resulting distribution over structure types in turn leads to a wide (semi)continuous distribution of spectral shifts, with both static and dynamic disorder contributing to the width. The time-averaged transfer of one or more atoms to the previously uncomplexed side of the molecule leads to increased red shifts relative to the smaller clusters. The amount of shift depends on the average number of atoms transferred. The single-sided monolayer-type structures are expected to yield only small shifts compared to the clusters with n = 6 and 7. Qualitatively, the red wing of the band is due to the sandwich-type clusters with an average of one atom on the second substrate side, which results in a differential red shift of ≈40 cm^{-1} relative to n = 6; the band center and high-frequency wing of the band are due to single-sided monolayer and bilayer-type clusters. A similar situation seems to prevail also for the n = 13 cluster.

For n = 9–11, the single-sided bilayer-type structures become energetically most favored. The increasing stability of bilayer structures for n = 9–11 leads to a *desolvation* of the partially solvated second substrate side and an increasing differential *blue shift* compared to n = 8. Significantly, the n = 11 cluster exhibits the same red shift as the n = 6 cluster, indicating that the number of first-layer solvent atoms is similar. On the average a smaller fraction of the population will be bound to the second substrate side for n = 9–11; it is this fraction that gives rise to the extended exponential red wing of the band that is observed.

In bilayer structures, the degree of structural disorder is much larger in the second, less tightly bound solvent layer. Due to the much weaker substrate → second-layer interaction, second-layer disorder has much smaller influence on the electronic spectrum that disorder in the first solvent layer. Hence the increase of the relative fraction of bilayer structures leads to a decrease of first-layer disorder and thus to a *relative decrease* in bandwidth for n = 9–11, as is experimentally observed. The increase in red shift and bandwidth from n = 11 to n = 13 indicates that sandwich-type structures again become favorable, in agreement with the low side-crossing temperatures found in the simulations.

Order–Disorder Transitions. The MC simulations indicate that the relative populations of various structure types is a sensitive function of both cluster size and temperature. Interconversion occurs mainly by side exchange and second-layer promotion. Figure 16b shows the *inverse side-crossing temperatures*, $1/T_{SC}$, for clusters with n = 6–14. The initial structures in the Markov chain were single-sided monolayer for $n \leq 9$ and single-sided bilayer for $9 < n < 14$. One notes a strong size dependence of the transition temperatures and, more importantly, a *roughly parallel* trend of the inverse transition temperature to those of the experimental red shifts and bandwidths, shown in Figure 16a. This confirms the qualitative interpretation given above: the clusters with low side-exchange temperatures (high $1/T_{SC}$) show larger red shifts and bandwidths; conversely, the clusters with high side-exchange temperatures (low $1/T_{SC}$) exhibit smaller red shifts and narrower bands.

To summarize, the spectral features of intermediate-size clusters are determined by two complementary types of static/structural and dynamic behavior: (a) a wide distribution over all three structural types, with a large share of sandwich-type clusters, resulting in a large average red shift and large bandwidth (thermal excitation leads to second-layer promotion and bilayer-type structures, resulting in an extended blue spectral tail); (b) predominantly single-sided, bilayer-type structures, with differential blue shifts and narrow bandwidths (thermal excitation leads to side-crossing and a red spectral tail).

4. Large Solvent Clusters

4.1. Filling the First Solvent Shell

A concept that is fundamental to the physics and chemistry of liquids is that of a solvation layer or shell of solvent particles S that surround and are in van der Waals contact with a solute ion or molecule M. The existence and range of shell structure clearly show up in pair correlation functions of atomic or simple molecular liquids, as obtained by X-ray or neutron scattering analysis. The special case of solvation shells follows by analogy from the analysis of partial radial distribution functions of S around M. In liquids, solvent molecules rapidly exchange between specific shells, leading to a nonvanishing particle density between shells and a continuous albeit highly structured distribution of molecular separations.[67]

The question whether solvent shell structure is experimentally observable in clusters is therefore important and fascinating. The carbazole·Ar_n system provides several independent indications of solvent shell filling:

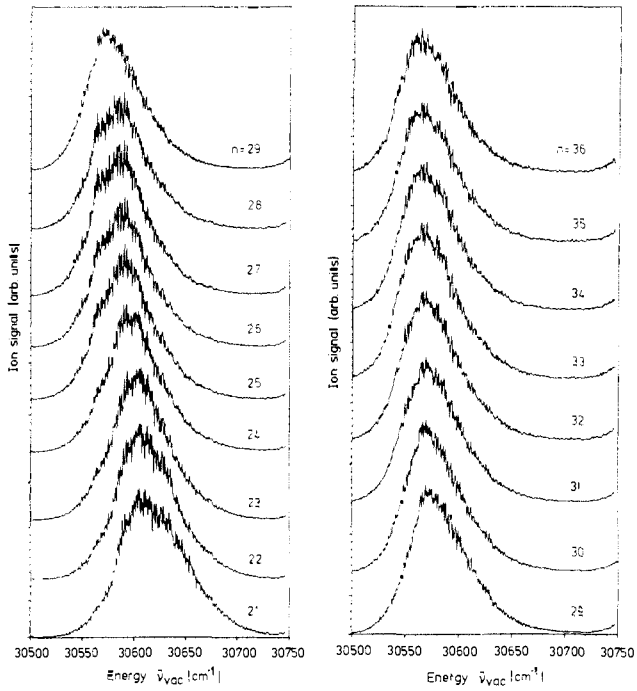

Figure 19. Resonant two-photon ionization spectra of carbazole·Ar_n, with n = 21–36 over the spectral region of the electronic origins.

Band Shapes. In Figure 19 we show the R2PI spectra of large carbazole·Ar_n clusters with n = 21–36. At first glance, the spectra seem quite broad and similar to each other. Closer examination reveals that there is a distinct changeover of spectral structure between n = 28 and n = 29 and that the clusters with n = 29–31 show a peak with a clear onset on the low-frequency side. These features imply that the n = 29–31 clusters attain a narrower, more homogeneous distribution of structures, suggesting shell closure.

Solvent Cluster Distributions and Layer Filling. The intensity distribution of the cluster ions produced by the R2PI process were obtained by integrating over the electronic origin transitions (Figure 19). In the absence of fragmentation these correspond to the neutral-cluster distributions. For given stagnation pressure and nozzle conditions, one obtains a distribution as shown in Figure 20; this distribution shows a characteristic intensity maximum at n = 29 and 30, followed by a drop between n = 30 and n = 31. Although the overall form of the distribution can be changed by altering the expansion conditions, the intensity maximum of the n = 29 and 30 clusters as well as the intensity drop from n = 30 to n = 31 always remains conspicuous. We propose that the special intensity of the n = 29 and 30 clusters is related to their high differential stability, relative to both the smaller and larger clusters and *that this differential stability is due to solvent shell closure.*

Red Shifts. As discussed in section 3.1, the red-shift development for n = 1–35 (Figure 3) allows a rough separation of the filling of the first solvent shell into two halves: solvation of one side of the substrate molecule is complete at $n \approx 14$ with a red shift level of $\delta\nu = 120 \pm 15$ cm^{-1}; solvation of the second side of the carbazole substrate is complete at $n \approx 29$–30, with a first-layer "terminal" red shift level of $\delta\nu = 240$ cm^{-1} = 2×120 cm^{-1}. Note, however, that the red shift criterion is somewhat biased, since structural changes of the

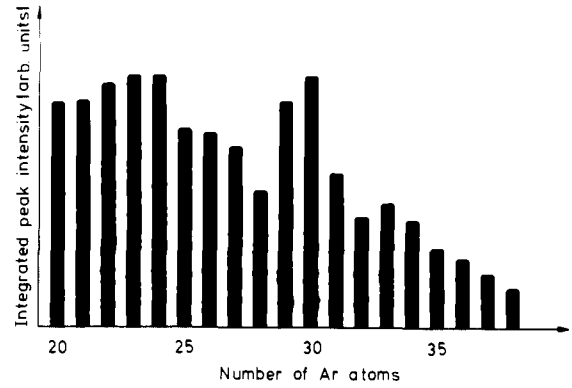

Figure 20. Carbazole·Ar_n^+ cluster ion intensity distribution obtained by integrating over the electronic origins of Figure 19. Note the increased intensities of n = 29 and 30 as well as the sharp intensity drop between 30 and 31.

cluster occurring above the central aromatic part of the molecule influence the shift much more than changes in the periphery of the solvent cluster. Thus, at n = 19 about 83% of the terminal red shift is achieved, yet the carbazole molecule is only solvated to an extent of ≈60–65% by space-filling criteria.

The solvent atom distribution and binding energies for the clusters with n = 28–33 were also examined by MD and MC simulations, which yield a number of interesting conclusions. First from purely geometrical, close-packing considerations, the first solvent shell was predicted to close at n = 32. This is quite close to the value of n = 29–30 inferred from the cluster intensity distributions. An example of the spatial probability density distribution for n = 30 and T = 25 K is shown in Figure 21a.

Second, the differential binding energies $\Delta V_{n,n-1}$, i.e., the binding energy increase on adding an atom to cluster size n – 1 to form cluster of size n, is quite high for the series n = 29–32, on the order of 570–610 cm^{-1}, but decreases precipitously from 32 to 33, as $\Delta V_{(33,32)}$ = 371 cm^{-1}. Third, within the series n = 28–32, the highest differential binding energies are obtained for the 28 → 29 growth step. The results of the simulations are thus in good agreement with the hypothesis of differential stability as the controlling factor for cluster distributions.

In general, then, in the carbazole·Ar_n system, solvent shell closure can be placed at n = 29–32 by three different experimental criteria. It is important to note that the meaning of "closure" can be slightly different, depending on the criterion chosen.

Venturing beyond the first solvent shell, we can inquire as to what the structural and spectroscopic effects expected for the second and further shells might be. Regarding solvent cluster structures, we expect the continuation of wetting–nonwetting transitions. Thus, depending on solute, solvent, and temperature, also for large multilayered solvent clusters nonwetting cluster structures with an unclosed first shell may be competitive with clusters exhibiting a closed first shell. The spectroscopic effects may still be quite large.

The contributions of second and further shells to the spectral shift die out quickly. Depending on the size of the solute and the relative contributions of inductive or dispersive parts to the shift, the distance dependence is $\sim r^{-4}$ to r^{-6} (see refs 23 and 30 and references therein). For carbazole, the total contribution of the second shell,

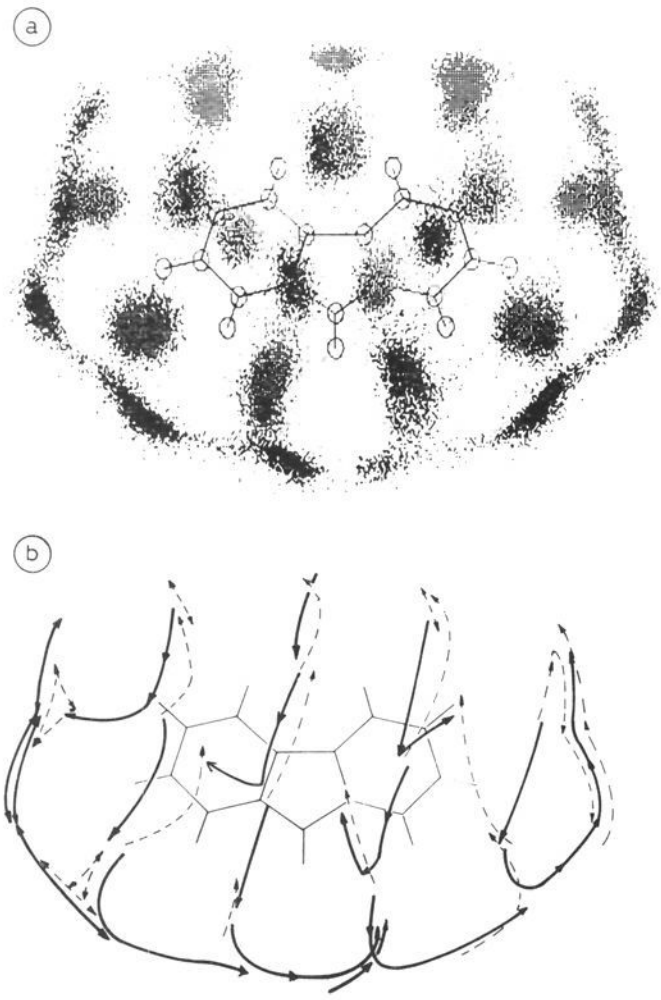

Figure 21. Monte Carlo simulations of the carbazole·Ar_{30} solvent cluster with a near-filled solvent shell. (a) Spatial probability density distribution at T = 25 K. The probability density is plotted in the half-space above the substrate only; the darker shading indicates atoms that remained on the top surface during the simulation run, the lighter shading indicates atoms that moved up from the lower surface. (b) Schematic diagram indicating the (stochastic) motion undergone by the individual atoms in the same MC simulation, showing rotational diffusion of the cluster around the solute; full arrows indicate motions of atoms in the upper half-space, and dashed lines indicate atomic motions in the lower half-space.

containing 50–60 atoms, is estimated to be ≈10% of that of the first. Regarding spectroscopic data for the $n \rightarrow \infty$ limit, matrix spectroscopy experiments are currently under way.[72] We note that there is also an effect of the solvent on the absolute oscillator strength of the solute electronic transition. In the bulk limit these are the well-known corrections to the radiative lifetime τ_{rad} by the refractive index ρ as $\tau_{rad} = \tau_{fl}/\phi_{fl}$ = constant/ρ^2.[73,74]

4.2. From Simplicity to Complexity and Back

When overviewing the development of the electronic spectra for n = 1–32, we note a curious and important feature: the complexity of the spectra first increases with size, peaking for the medium-sized clusters (size range n = 8–20), but decreases thereafter. An illustration of this behavior is seen in Figure 3b, which shows the bandwidth $\Delta\nu$ as a function of n. Although the bandwidth is only a crude measure of spectral complexity, it is clearly seen that the bandwidth is low at small cluster size, rises rapidly for n = 6–8, goes through a series of oscillations for n = 6–20, and thereafter decreases to a relatively modest $\Delta\nu \approx 50$ cm^{-1} for $n \geq 20$.

The geometrical and dynamical characteristics of the *small* solvent clusters ($n \leq 7$) are dominated by the quasi-planar substrate, which induces 2-D structures and, at finite temperature, 2-D order–disorder transitions (see sections 3.2 to 3.4). The complexity of the system is restricted, and the features of the system can be discussed in terms of nearly flat monolayer structures and their associated order–disorder transitions. Starting at $n \approx 7$, 3-D structures and disorder become important, and the polymorphism (single-sided, double-sided, monolayer, and bilayer structures) and associated transitions lead to an increase in the complexity of the spectra.

Above $n \approx 21$, the solvent "polar caps" can make contact, and the collective stabilization effects drive the solvent toward a single solvent shell of toroidal or near-ellipsoidal shape. The system typically reverts from 3-D to quasi-2-D behavior. For large clusters (n > 21), there are only two important low-temperature transitions: (1) diffusion of vacancies within the solvent shell (this is the "hole" analogue of the isomerization transitions of small clusters) and (2) rotational diffusion of the whole solvent cluster around the solute molecule, or in a complementary view the rotational "tumbling" of the solute within its single solvent shell. The solvent atom motions are purely tangential to the solute molecule surface, analogous to the surface-decoupling transitions of the small solvent clusters (see Figure 21b). For the "filled" solvent shell around n = 30–32, the vacancy–diffusion mechanism no longer exists, and the lowest remaining order–disorder transition is rotational diffusion. Since the main effect of this motion is to permute atoms between solute-fixed "solvation sites", the spectral effects are expected to be quite modest, leading to relatively simple spectra.

5. Conclusions and Outlook

Cold solute–solvent clusters can be prepared in high-density supersonic expansions followed by isolation in a collision-free high-vacuum environment. By changing the concentration of the "solvent" rare gas or the total backing pressure, one can build increasingly large clusters. Laser two-photon ionization with mass spectrometric detection has allowed *size-specific electronic spectra* of solute–solvent clusters to be measured over a wide size range.

The vibronic band structures exhibit a great variety of fine structure, shifts, bandwidths, and band shapes, which reflect both static and dynamic aspects of the behavior of the microsolvent shell on or surrounding the planar chromophore. Especially notable are a number of discontinuous and nonadditive changes in the spectra: (i) appearance of broad, semicontinuous bands starting at n = 4; (ii) coexistence of narrow and broad bands in the size range n = 4–7; (iii) complete broadening of vibronic bands for n = 8 and 9; (iv) reappearance of narrow-band features for n = 11, 14, and 20; (v) large variations in red shifts and bandwidths for n = 6–14; (vi) especially intense cluster abundances and relatively sharp spectra for n = 29 and 30 ("magic" numbers).

The *theoretical methods* that are employed to predict and analyze the properties of solvent clusters must allow a description of the clusters at finite temperature, far from the zero-energy "equilibrium" structure, and undergoing rapid isomerization and structural fluctuations. Conventional theoretical methods of treating molecular structure and dynamics are based on rigid-structure, harmonic oscillator concepts and are of little help except for the treatment of the smallest clusters

TABLE II. Some Structural and Dynamic Characteristics of Carbazole•Ar_n Solvent Clusters

size range	properties
1–3	same sided (n + 0), C_s symmetry; well-defined average structure; large-amplitude vibrational motions, typical frequencies $\omega_{x,y} \approx$ 1–20 cm^{-1} (in plane), $\omega_z \approx$ 40–50 cm^{-1} (out of plane)
4–6	same sided (n + 0), nonsymmetric; coexistence of surface-locked and -decoupled cluster structures; surface-decoupling transitions $T_{sd} \approx$ 14–20 K
7, 8	same-sided and double-sided (n + 1) structures; at experimental temperatures (20–25 K) completely surface decoupled; side-crossing transitions $T_{sc} \approx$ 20–23 K
9–14	range of same-sided (monolayer, bilayer) and double-sided structures; approximately half-solvated solute at n = 14; combination of side-crossing and second-layer promotion, amounting to wetting–nonwetting transitions
15–28	solvation of second side of solute
29–32	closure of first solvent shell

at low temperatures. Statistical mechanical computer simulation techniques (Monte Carlo, molecular dynamics), which were developed and applied for the study of fluids, have turned out to be of great predictive and heuristic value. They have allowed us to predict characteristic size- and temperature-dependent properties of the solvent clusters and to rationalize in detail the spectral features (see also Table II):

Structures. For n = 1–3, unique minima corresponding to symmetric, well-localized, near-rigid structures were found. For $n \geq 4$, the number of locally stable cluster isomers increases very rapidly, and many isomers become competitive with the minimum-energy structure. Cluster growth proceeds on one side of the substrate up to n = 7. For $7 \leq n \leq 21$, three structural types (monolayer, bilayer, and sandwich) become energetically competitive. From n = 21 to n = 30, sandwich-type structures are dominant. Filling of the first solvent shell is completed by n = 31 or 32. The MC simulations show that certain characteristic sites are preferentially solvated, even at temperatures for which the clusters are completely liquidlike (cf. Figures 8d, 11b, and 21a). Thus the large aromatic solute can *imprint its molecular shape* on the first solvent layer.

Order–Disorder Transitions. The evolution of cluster structure and dynamics from low-temperature, rigid or solidlike clusters to high-temperature, fluxional or liquidlike clusters proceeds through a series of order–disorder or microscopic "phase" transitions. So far, the simulations have revealed seven different transition types, which are characterized by rapid increases of the structural order parameters σ and δ, as a function of temperature. This hierarchy of transitions constitutes the complete "melting" process of the finite solvent cluster; the actual series of transitions involved depends on cluster size and structural type. We classify the different order–disorder transitions according to (I) loss of cluster/substrate structural correlation and (II) loss of intracluster structural correlation (see also Table I).

(I) Cluster–substrate type transitions: (*Ia*) *Isomerization transitions* involve jumps of one or a few atoms between different substrate-fixed solvation sites, the rest of the cluster remaining rigidly solute fixed. (*Ib*) *Racemization transitions* occur as collective motions of all atoms in the cluster that interconvert mirror-symmetric structures (defined in a substrate-fixed frame). The atomic displacements are typically highly complex translational motions, approximately parallel to the substrate surface. (*Ic*) *Surface-decoupling transitions* involve complete loss of cluster–substrate correlation parallel to the substrate surface, allowing cyclic permutation of cluster atoms over all available solvation sites on one side. (*Id*) *Side-crossing transitions* entail the crossing of one of several atoms to the opposite surface of the substrate. (*Ie*) *Second-layer promotion transitions* involve the excitation of one or several atoms to the second solvent layer. Both side-crossing and second-layer promotions can combine to yield wetting–nonwetting transitions, in which a bi- or multilayer cluster droplet adsorbed to one substrate surface can spread to wet both solute surfaces.

(II) Intracluster type transitions: (*IIa*) *Rigid–fluxional transitions* involve partial (rigid–fluxional) loss of intracluster bond orientational correlation and increases in bond length fluctuations. (*IIb*) *Melting transitions* occur when the bond length fluctuations of all atoms in the cluster increase above 10%. We note that the intracluster type order–disorder transitions observed in solvent clusters are also relevant to the understanding of transitions in pure (undoped) clusters. A second type of classification is also possible according to dimensionality: for the monolayer clusters (n = 1–6) the relevant transitions are quasi-two-dimensional, while for the larger clusters ($n \geq 7$) three-dimensional transitions are important.

With the results of the simulations, the discontinuous spectroscopic effects of structural features and of the order–disorder transitions can be interpreted: (i) the appearance of spectral broadening of the vibrationless 0_0^0 bands at n = 4 is due to substrate–cluster (rigid–fluxional and surface-decoupling) transitions; (ii) the coexistence of structured and broad bands for n = 4–7 constitutes clear experimental evidence for coexistence of rigid and fluxional finite-size clusters in a canonical-type ensemble; (iii) the complete broadening of vibronic bands for n = 8 and 9 is due to a multiplicity of structures and the occurrence of side-crossing and second-layer-promotion transitions; (iv) the appearance of narrow spectral features for $n \approx$ 11, 14, and 20 reflects the formation of bilayer structures with near-solidified first layers; (v) the semicyclic developments of red shifts and bandwidths for n = 6–14 is based on corresponding shifts in relative stability (binding energy) between bilayer-type and sandwich-type structures; (vi) the enhancement of cluster abundances at $n \approx$ 30 is due to solvent shell closure.

Further improvements in the interpretation of the spectra will rest on direct simulation of the spectroscopic band shapes. Work using the classical Franck–Condon principle coupled with the MC simulation technique is presently under way.[68] A different type of improvement is necessary for the analysis of the "small" solvent clusters with n = 2–6, which exhibit discrete bands corresponding to quasi-periodic motions at low internal energy, but broad bands, corresponding to classically chaotic motion at higher energy. Semiclassical techniques are currently being applied to this problem.[70]

While the types of order–disorder transitions observed experimentally are specific for the chosen substrate and are by no means universal as regards char-

acteristic temperature and size ranges, the types of transitions as outlined in the classification above should be fairly comprehensive for planar aromatic solutes in simple atomic and even compact nonpolar molecular solvents (CH_4, CF_4, etc.). Further insights into the details of molecular solvation will be forthcoming from the study of other solutes and solvent atoms or molecules.[68,71,72]

Acknowledgments. We are indebted to our colleagues Rolf Bombach, Evi Honegger, and Richard Knochenmuss for their collaboration on this project and to Profs. Uzi Even and Joshua Jortner (Tel-Aviv University, Israel) for many stimulating conversations. Our research is financially supported by the Schweizerischer Nationalfonds.

References

(1) Smalley, R. E.; Wharton, L.; Levy, D. H.; Chandler, D. W. *J. Chem. Phys.* **1978**, *68*, 2487.
(2) Beck, S. M.; Liverman, M. G.; Monts, D. L.; Smalley, R. *J. Chem. Phys.* **1979**, *70*, 232.
(3) Levy, D. H. *Annu. Rev. Phys. Chem.* **1980**, *31*, 197.
(4) Levy, D. H. *Adv. Chem. Phys.* **1981**, *47*, 323.
(5) Amirav, A.; Even, U.; Jortner, J. *Chem. Phys. Lett.* **1979**, *67*, 9.
(6) Amirav, A.; Even, U.; Jortner, J. *J. Chem. Phys.* **1981**, *75*, 2489.
(7) Amirav, A.; Even, U.; Jortner, J. *J. Phys. Chem.* **1981**, *85*, 309.
(8) Amirav, A.; Even, U.; Jortner, J. *Chem. Phys.* **1982**, *67*, 1.
(9) Amirav, A.; Even, U.; Jortner, J. *Chem. Phys. Lett.* **1980**, *72*, 17.
(10) Amirav, A.; Even, U.; Jortner, J. *J. Phys. Chem.* **1982**, *86*, 3345.
(11) Even, U.; Amirav, A.; Leutwyler, S.; Ondrechen, M. O.; Berkovitch-Yellin, Z.; Jortner, J. *Faraday Discuss. Chem. Soc.* **1982**, *73*, 153.
(12) Leutwyler, S.; Even, U.; Jortner, J. *Chem. Phys. Lett.* **1982**, *86*, 439.
(13) Leutwyler, S.; Even, U.; Jortner, J. *J. Chem. Phys.* **1983**, *79*, 5769.
(14) Hays, T. R.; Henke, W.; Selzle, H. L.; Schlag, E. W. *Chem. Phys. Lett.* **1980**, *77*, 19.
(15) Hays, T. R.; Henke, W.; Selzle, H. L.; Schlag, E. W. *Z. Naturforsch. A* **1980**, *A35*, 1429.
(16) Fung, K. H.; Henke, W.; Selzle, H. L.; Schlag, E. W. *J. Phys. Chem.* **1981**, *85*, 3560. Fung, K. H.; Selzle, H. L.; Schlag, E. W. *Z. Naturforsch. A* **1981**, *A36*, 1338.
(17) Henke, W. E.; Yu, W.; Selzle, H. L.; Schlag, E. W.; Wutz, D.; Lin, S. *Chem. Phys.* **1985**, *92*, 187, **1985**, *97*, 205.
(18) Hopkins, J. B.; Powers, D. E.; Smalley, R. E. *J. Phys. Chem.* **1981**, *85*, 3739.
(19) Raitt, I.; Griffiths, A. M.; Freedman, P. A. *Chem. Phys. Lett.* **1981**, *80*, 225.
(20) Griffiths, A. M.; Freedman, P. A. *Chem. Phys.* **1981**, *63*, 469.
(21) Amirav, A.; Jortner, J. *Chem. Phys.* **1984**, *85*, 19.
(22) Amirav, A.; Sonnenschein, M.; Jortner, J. *Chem. Phys.* **1984**, *88*, 199.
(23) Leutwyler, S. *Chem. Phys. Lett.* **1984**, *107*, 284.
(24) Leutwyler, S. *J. Chem. Phys.* **1984**, *81*, 5480.
(25) Rademann, K.; Brutschy, B.; Baumgärtel, H. *Chem. Phys.* **1983**, *80*, 129.
(26) Amirav, A.; Even, U.; Jortner, J.; Dick, B. *Mol. Phys.* **1983**, *49*, 899.
(27) Dao, P. D.; Morgan, S.; Castleman, A. W., Jr. *Chem. Phys. Lett.* **1984**, *111*, 38.
(28) Dao, P. D.; Morgan, S.; Castleman, A. W., Jr. *Chem. Phys. Lett.* **1985**, *113*, 219.
(29) Doxtader, M. M.; Gulis, I. M.; Schwartz, S. A.; Topp, M. R. *Chem. Phys. Lett.* **1984**, *112*, 483.
(30) Kettley, J. C.; Palmer, T. F.; Simons, J. P. *Chem. Phys. Lett.* **1985**, *115*, 40. Kettley, J. C.; Palmer, T. F.; Simons, J. P.; Amos, A. T. *Chem. Phys. Lett.* **1986**, *126*, 107.
(31) Bösiger, J.; Leutwyler, S. *Chem. Phys. Lett.* **1986**, *126*, 238.
(32) Leutwyler, S.; Bösiger, J. *Z. Phys. Chem. (N.F.)* **1987**, *154*, 31.
(33) Bösiger, J.; Leutwyler, S. In *Large Finite Systems*; Jortner, J., Pullman, B., Eds.; Reidel: Dordrecht, 1987; pp 153–164.
(34) Bösiger, J.; Leutwyler, S. *Phys. Rev. Lett.* **1987**, *59*, 1895.
(35) Leutwyler, S.; Jortner, J. *J. Phys. Chem.* **1987**, *91*, 5558.
(36) Bösiger, J.; Leutwyler, S., submitted to *J. Chem. Phys.*
(37) Ondrechen, M. J.; Berkovitch-Yellin, Z.; Jortner, J. *J. Am. Chem. Soc.* **1981**, *103*, 6586.
(38) Gough, T. E.; Knight, D. G.; Scoles, G. *Chem. Phys. Lett.* **1983**, *97*, 155. Gough, T. E.; Mengel, M.; Rowntree, P. A.; Scoles, G. *J. Chem. Phys.* **1985**, *83*, 4958.
(39) Eichenauer, D.; LeRoy, R. J. *Phys. Rev. Lett.* **1986**, *57*, 2920; *J. Chem. Phys.* **1988**, *88*, 2898.
(40) LeRoy, R. J.; Shelley, J. C.; Eichenauer, D. In *Large Finite Systems*; Jortner, J., Pullman, B., Eds.; Reidel: Dordrecht, 1987; pp 165–172.
(41) Etters, R. D.; Kaelberer, J. B. *Phys. Rev. A* **1975**, *11*, 1068; *J. Chem. Phys.* **1977**, *66*, 3233, 5112.
(42) Briant, C. L.; Burton, J. J. *J. Chem. Phys.* **1975**, *63*, 2045.
(43) Quirke, N.; Sheng, P. *Chem. Phys. Lett.* **1984**, *110*, 63.
(44) Berry, R. S.; Jellinek, J.; Natanson, G. *Chem. Phys. Lett.* **1984**, *107*, 227.
(45) Berry, R. S.; Jellinek, J.; Natanson, G. *Phys. Rev. A* **1984**, *30*, 919.
(46) Jellinek, J.; Beck, T. L.; Berry, R. S. *J. Chem. Phys.* **1986**, *84*, 2783. Beck, T. L.; Jellinek, J.; Berry, R. S. *Ibid* **1987**, *87*, 545. Davis, H. L.; Jellinek, J.; Berry, R. S. *Ibid.* **1987**, *86*, 6456. Beck, T. L.; Berry, R. S. *J. Chem. Phys.* **1988**, *88*, 3910. Beck, T. L.; Leitner, D. M.; Berry, R. S. *J. Chem. Phys.* **1988**, *89*, 1681.
(47) Honeycutt, J. D.; Andersen, H. C. *J. Phys. Chem.* **1987**, *91*, 4950.
(48) Etters, R. D.; Danilowicz, R. *J. Chem. Phys.* **1979**, *71*, 4767.
(49) Barker, J. A. In *Rare Gas Solids*; Klein, M. L., Venables, J. A., Eds.; Academic Press: New York, 1976; Vol 1, Chapter 4. Barker, J. A. *Phys. Rev. Lett.* **1986**, *57*, 230.
(50) Doran, M. B.; Zucker, I. J. *J. Phys. C* **1971**, *4*, 307.
(51) Aziz, R. A.; Chen, H. H. *J. Chem. Phys.* **1977**, *67*, 5719. Aziz, R. A. In *Inert Gases*; Klein, M. L., Ed.; Springer-Verlag: Berlin, 1984.
(52) Michels, A.; Wijker, H.; Wijker, H. *Physica* **1949**, *15*, 627.
(53) Alder, B. J.; Wainwright, T. E. *J. Chem. Phys.* **1957**, *27*, 1208. Alder, B. J.; Wainwright, T. E. *J. Chem. Phys.* **1959**, *31*, 459. Rahman, A. *Phys. Rev. A* **1964**, *136*, 405.
(54) Metropolis, N.; Rosenbluth, A. W.; Rosenbluth, M. N.; Teller, A. H.; Teller, E. *J. Chem. Phys.* **1953**, *21*, 1087.
(55) For recent overviews of MD and MC simulations, see, e.g.: Allen, M. P.; Tildesley, D. J. *Computer Simulation of Liquids*; Oxford University Press: Oxford, 1987. Binder, K., Ed. *Monte-Carlo Methods in Statistical Physics*; Springer: Berlin, 1979. Kehr and Binder have pointed out that the Markov chain of system configurations (configuration space points) $R \rightarrow R' \rightarrow R''$, generated one after the other from the respective previous states, can be interpreted as a stochastic "dynamic" evolution of the system if a time t is associated with the sequential label of these states. The introduction of a time unit is arbitrary; a convenient definition is the Monte Carlo step per particle. No real-time or true dynamic information can be obtained, but the low-energy correlated atomic motions that lead to the order–disorder transitions are readily apparent. See also: Kehr, K. W.; Binder, K. In *Applications of the Monte-Carlo Method in Statistical Physics*; Binder, K., Ed.; Springer: Berlin, 1984; pp 181–221.
(56) Pawlow, P. *Z. Phys. Chem.* **1909**, *65*, 1.
(57) Borel, J.-P. *Surf. Sci.* **1981**, *106*, 1.
(58) Bree, A.; Zwarich, R. *J. Chem. Phys.* **1968**, *49*, 3344, 3355.
(59) Henke, W. E.; Yu, W.; Selzle, H. L.; Schlag, E. W.; Wutz, D.; Lin, S. H. *Chem. Phys.* **1985**, *97*, 205.
(60) Vilches, O. E. *Annu. Rev. Phys. Chem.* **1980**, *31*, 463.
(61) Chinn, M. D.; Fain, S. C. *Phys. Rev. Lett.* **1977**, *39*, 140.
(62) Hanson, F.; McTague, J. P. *J. Chem. Phys.* **1980**, *7*, 6363.
(63) Moncton, D.; Stephens, P.; Birgenau, R.; Horn, P.; Brown, G. *Phys. Rev. Lett.* **1981**, *46*, 1533.
(64) Nielson, M.; Als-Nielsen, J.; Bohr, J.; McTague, J. P. *Phys. Rev. Lett.* **1981**, *47*, 582.
(65) Abraham, F. F.; Koch, S. W.; Rudge, W. E. *Phys. Rev. Lett.* **1982**, *49*, 1830.
(66) Abraham, F. F.; Rudge, W. E.; Auerbach, D. J.; Koch, S. W. *Phys. Rev. Lett.* **1984**, *52*, 445.
(67) See, e.g.: Friedman, H. L. *Annu. Rev. Phys. Chem.* **1981**, *32*, 179. Enderby, J. E. *Ibid.* **1983**, *34*, 155. Hunt, J. P.; Friedman, H. L. *Prog. Inorg. Chem.* **1983**, *30*, 359.
(68) Leutwyler, S.; Bösiger, J. *J. Chem. Phys.*, in press.
(69) Imry, Y. *Phys. Rev.* **1980**, *B21*, 2042. Pearson, E. M.; Halicioglu, T.; Tiller, W. A. *Phys. Rev.* **1985**, *A32*, 3030. Bixon, M.; Jortner, J., in press.
(70) Mukamel, S. *J. Chem. Phys.* **1982**, *77*, 173. Islampour, R.; Mukamel, S. *Chem. Phys. Lett.* **1984**, *107*, 239.
(71) (a) Even, U.; Ben-Horin, N.; Jortner, J. *Phys. Rev. Lett.* **1989**, *62*, 140. (b) Hahn, M. Y.; Whetten, R. L. *Phys. Rev. Lett.* **1988**, *61*, 1190.
(72) Tramer, A. CNRS, Orsay, private communication.
(73) Olmsted, J. *Chem. Phys. Lett.* **1976**, *38*, 287.
(74) Hirayama, S.; Phillips, D. *J. Photochem.* **1980**, *12*, 139.